

UNIVERSITÀ DEGLI STUDI DI PADOVA

---

DIPARTIMENTO DI INGEGNERIA INDUSTRIALE  
CORSO DI LAUREA MAGISTRALE IN INGEGNERIA AEROSPAZIALE

*Dynamic analysis  
of thin-film solar panels  
on small satellites*

RELATORE

*Prof. Ing. Alessandro Francesconi*

LAUREANDA

*Laura Bettiol*

1039513

CORRELATORE

*Ing. Francesco Branz*

---

ANNO ACCADEMICO 2013–2014



# ABSTRACT

Thin-film solar panels for space applications have been studied since the 1960s, but the important issue of degradation over time discouraged their use. In recent years many efforts have been done in order to improve this promising technology, because of its advantages in terms of lower cost and higher power density with respect to traditional bulk solar panels.

The main drawback of this technology is the extreme flexibility that implies very low first natural frequencies for the panels. Such frequencies can in some cases match with orbital frequencies or can be excited by typical maneuvers leading to important instability conditions, in which power production and vehicle attitude are compromised.

This thesis discusses the effects of the main orbital disturbances on the attitude of a small spacecraft with two large flexible appendages. Different orbital configurations were simulated with a numerical multi-body code. The flexible components have been modeled with the lumped mass method. The panels are therefore discretized into a number of rigid bodies, connected to each other by rotational joints, while the spacecraft is thought as a single rigid body. The simulations are performed with variable panels thickness. The collected results are in terms of torques necessary for the satellite to keep a certain attitude and torques transmitted from the panels to the central body. Simulations have been performed also including a distributed control action provided by smart active films along the panel length. A comparison between the free and the controlled systems is presented and advantages and drawbacks are assessed in detail.



# ABSTRACT

I pannelli solari a film sottile per applicazioni spaziali vengono studiati già dagli anni '60, ma il loro utilizzo fu inizialmente scoraggiato da importanti problemi di degradazione nel tempo. Negli ultimi anni si stanno facendo molti sforzi per migliorare le performance di questa tecnologia promettente, che consente di avere una serie di vantaggi tra i quali un costo inferiore e una potenza specifica superiore a quella dei pannelli solari tradizionali.

Lo svantaggio principale di questa tecnologia è la sua estrema flessibilità, che implica frequenze naturali dei pannelli molto basse. Queste frequenze possono in alcuni casi corrispondere a frequenze orbitali o possono essere eccitate da manovre tipiche che possono portare a condizioni di instabilità importante, in cui la produzione di potenza e l'assetto del veicolo vengono compromessi.

Questa tesi discute gli effetti dei principali disturbi orbitali sull'assetto di un piccolo satellite con due grandi appendici flessibili. Sono state simulate diverse configurazioni orbitali con un simulatore multi-body. I componenti flessibili sono stati modellati tramite il metodo delle masse concentrate. Perciò i pannelli sono stati discretizzati in un certo numero di corpi rigidi connessi l'uno all'altro tramite giunti rotazionali, mentre il corpo centrale del satellite è pensato come un'unica massa. Le simulazioni sono state fatte variando lo spessore dei pannelli. I risultati sono presentati in termini di coppie necessarie al sistema di controllo d'assetto del corpo centrale per mantenere il corretto puntamento e coppie trasmesse dal pannello al corpo centrale. Le simulazioni sono state fatte anche includendo un sistema di controllo delle oscillazioni distribuito nell'intera lunghezza dei pannelli, che può essere pensato come un film di materiale *smart*. Infine, viene fatto un confronto tra il sistema irrigidito e quello controllato, presentando i relativi vantaggi e svantaggi in dettaglio.



# CONTENTS

1	INTRODUCTION	1
1.1	Background	2
1.2	Solar cells layout	3
1.2.1	Inorganic materials	3
1.2.2	Polymer materials	4
1.3	The substrate	4
1.4	Cost benefits of thin-film technology	5
1.5	Performances	6
1.5.1	Efficiency	6
1.5.2	Radiation resistance	6
1.5.3	Specific power	8
1.5.4	Temperature coefficient	8
1.6	Motivations	9
2	MODEL DEFINITION	11
2.1	Geometry and material	11
2.2	Model description	11
2.2.1	Satellite orientation	12
2.2.2	Masses	12
2.2.3	Joints	13
2.2.4	Dimensions of the panels	15
2.2.5	Power production	20
2.3	Orbital disturbances	20
2.3.1	Drag	20
2.3.2	Solar radiation pressure	23
2.3.3	Gravity gradient	24
2.3.4	Magnetic field	27
3	SIMULATIONS WITHOUT VIBRATIONS CONTROL SYSTEM	31
3.1	Simulations with 25 $\mu\text{m}$ thick panels	32
3.2	Simulations with panels of different thicknesses	33
3.2.1	Simulations in low LEO	34
3.2.2	Simulations in high LEO	35
4	SIMULATIONS WITH ACTIVE VIBRATIONS CONTROL SYSTEM	45
4.1	Results of the simulations with an actively controlled system	46

4.1.1	Simulations in low LEO	47
4.1.2	Simulations in high LEO	49
5	COMPARISON BETWEEN THE SIMULATED SYSTEMS	65
5.1	Torques	65
5.2	Mass	66
5.3	Required power	69
6	PROPOSAL OF AN INNOVATIVE CONTROL SYSTEM	73
6.1	Piezoelectric polymers	73
6.2	Dielectric elastomers	75
7	CONCLUSION	77
	BIBLIOGRAPHY	79

# LIST OF FIGURES

Figure 1.1	Schematic drawing of a flexible CIGS TFSC. Not to scale. [2]	3
Figure 1.2	Comparison between the best research cell efficiencies up to 2013. <a href="http://www.nrel.gov/ncpv/images/efficiency_chart.jpg">http://www.nrel.gov/ncpv/images/efficiency_chart.jpg</a>	7
Figure 1.3	Specific power of lightweight solar array with thin-film, thin crystalline silicon and crystalline GaAs solar cells as a function of conversion efficiency. [23]	8
Figure 2.1	Example of a joint subsystem.	16
Figure 2.2	The central body (orange) is connected through the joints (light blue) with the panels (green).	17
Figure 2.3	First natural frequency of a 5.51 m long panel.	19
Figure 2.4	Second natural frequency of a 5.51 m long panel.	19
Figure 2.5	Instantaneous power production of the two simulated 500 $\mu\text{m}$ thick panels in the two attitude configurations at 300 km height.	21
Figure 2.6	Drag force at 300 km for panels of different thicknesses.	22
Figure 2.7	Drag force at 500 km for panels of different thicknesses.	22
Figure 2.8	Drag force at 750 km for panels of different thicknesses.	22
Figure 2.9	Force exerted by solar radiation pressure at different altitudes on a 500 $\mu\text{m}$ thick panel in equatorial orbit with inertial attitude, in the <i>World</i> CS.	24
Figure 2.10	X component (along the local vertical) of the gravity gradient force at the tip of a 25 $\mu\text{m}$ thick panel at different altitudes.	26

Figure 2.11	X component (along the local vertical) of the gravity gradient force at the tip of a 500 $\mu\text{m}$ thick panel at different altitudes. 26
Figure 2.12	Components of the magnetic field at different altitudes. 29
Figure 2.13	Components of the torque due to the interaction of the panels with the magnetic field at different altitudes. 29
Figure 3.1	Behavior of 25 $\mu\text{m}$ thick panels subjected to drag force at 300 km height, at the beginning of the simulation. 32
Figure 3.2	Displacements of the left tip at 300 km altitude with inertial attitude (see table 3.1). 37
Figure 3.3	Displacements of the right tip at 300 km altitude with inertial attitude (see table 3.1). 37
Figure 3.4	Torques transferred from the left panel to the central body at 300 km altitude with inertial attitude (see table 3.1). 38
Figure 3.5	Torques transferred from the right panel to the central body at 300 km altitude with inertial attitude (see table 3.1). 38
Figure 3.6	Control torques on the satellite at 300 km altitude with inertial attitude (see table 3.1). 38
Figure 3.7	Displacements of the left tip at 300 km altitude (see table 3.2). 39
Figure 3.8	Displacements of the right tip at 300 km altitude (see table 3.2). 39
Figure 3.9	Torques transferred from the left panel to the central body at 300 km altitude with nadir pointing attitude (see table 3.2). 40
Figure 3.10	Torques transferred from the right panel to the central body at 300 km altitude with nadir pointing attitude (see table 3.2). 40
Figure 3.11	Control torques on the satellite (see table 3.2). 40
Figure 3.12	Displacements of the left tip at 750 km altitude (see table 3.3). 41

Figure 3.13	Displacements of the right tip at 750 km altitude (see table 3.3).	41
Figure 3.14	Torques transferred from the left panel to the central body (see table 3.3).	42
Figure 3.15	Torques transferred from the right panel to the central body (see table 3.3).	42
Figure 3.16	Control torques on the satellite (see table 3.3).	42
Figure 3.17	Displacements of the left tip at 750 km altitude (see table 3.4).	43
Figure 3.18	Displacements of the right tip at 750 km altitude (see table 3.4).	43
Figure 3.19	Torques transferred from the left panel to the central body (see table 3.4).	44
Figure 3.20	Torques transferred from the right panel to the central body (see table 3.4).	44
Figure 3.21	Control torques on the satellite (see table 3.4).	44
Figure 4.1	PD controller block system.	46
Figure 4.2	Displacements of the left tip at 300 km altitude with inertial attitude with controlled systems (see table 4.2).	51
Figure 4.3	Displacements of the right tip at 300 km altitude with inertial attitude with controlled systems (see table 4.2).	51
Figure 4.4	Torques transferred from the left panel to the central body at 300 km altitude with inertial attitude (see table 4.2).	52
Figure 4.5	Torques transferred from the right panel to the central body at 300 km altitude with inertial attitude (see table 4.2).	52
Figure 4.6	Control torques on the satellite at 300 km altitude with inertial attitude (see table 4.2).	53
Figure 4.7	Control torques exerted by the control system on the connecting joint between the left panel and the central body (see table 4.2).	53
Figure 4.8	Control torques exerted by the control system on the connecting joint between the right panel and the central body (see table 4.2).	53

Figure 4.9	Displacements of the left tip at 300 km altitude with nadir pointing attitude with controlled systems (see table 4.3).	54
Figure 4.10	Displacements of the right tip at 300 km altitude with nadir pointing attitude with controlled systems (see table 4.3).	54
Figure 4.11	Torques transferred from the left panel to the central body at 300 km altitude with nadir pointing attitude (see table 4.3).	55
Figure 4.12	Torques transferred from the right panel to the central body at 300 km altitude with nadir pointing attitude (see table 4.3).	55
Figure 4.13	Control torques on the satellite at 300 km altitude with nadir pointing attitude (see table 4.3).	56
Figure 4.14	Control torques exerted by the control system on the connecting joint between the left panel and the central body (see table 4.3).	56
Figure 4.15	Control torques exerted by the control system on the connecting joint between the right panel and the central body (see table 4.3).	57
Figure 4.16	Displacements of the left tip at 750 km altitude with inertial attitude with controlled systems (see table 4.5).	57
Figure 4.17	Displacements of the right tip at 750 km altitude with inertial attitude with controlled systems (see table 4.5).	58
Figure 4.18	Torques transferred from the left panel to the central body at 750 km altitude with inertial attitude (see table 4.5).	58
Figure 4.19	Torques transferred from the right panel to the central body at 750 km altitude with inertial attitude (see table 4.5).	59
Figure 4.20	Control torques on the satellite at 750 km altitude with inertial attitude (see table 4.5).	59

- Figure 4.21 Control torques exerted by the control system on the connecting joint between the left panel and the central body (see table 4.5). 60
- Figure 4.22 Control torques exerted by the control system on the connecting joint between the right panel and the central body (see table 4.5). 60
- Figure 4.23 Displacements of the left tip at 750 km altitude with nadir pointing attitude with controlled systems (see table 4.6). 61
- Figure 4.24 Displacements of the right tip at 750 km altitude with nadir pointing attitude with controlled systems (see table 4.6). 61
- Figure 4.25 Torques transferred from the left panel to the central body at 750 km altitude with nadir pointing attitude (see table 4.6). 62
- Figure 4.26 Torques transferred from the right panel to the central body at 750 km altitude with nadir pointing attitude (see table 4.6). 62
- Figure 4.27 Control torques on the satellite at 750 km altitude with nadir pointing attitude (see table 4.6). 63
- Figure 4.28 Control torques exerted by the control system on the connecting joint between the left panel and the central body (see table 4.6). 63
- Figure 4.29 Control torques exerted by the control system on the connecting joint between the right panel and the central body (see table 4.6). 64
- Figure 5.1 Comparison between the displacements and the torques needed to control the satellite in the stiffened case with 500  $\mu\text{m}$  thick panels and three entirely controlled systems in low LEO with inertial attitude. 67

- Figure 5.2 Comparison between the displacements and the torques needed to control the satellite in the stiffened case with 500  $\mu\text{m}$  thick panels and three entirely controlled systems in low LEO with nadir pointing attitude. 67
- Figure 5.3 Comparison between the displacements and the torques needed to control the satellite in the stiffened cases with 200  $\mu\text{m}$  and 500  $\mu\text{m}$  thick panels and three entirely controlled systems in high LEO with inertial attitude. 68
- Figure 5.4 Comparison between the displacements and the torques needed to control the satellite in the stiffened cases with 200  $\mu\text{m}$  and 500  $\mu\text{m}$  thick panels and three entirely controlled systems in high LEO with nadir pointing attitude. 68
- Figure 5.5 Comparison between the displacements and the masses of the systems in the stiffened case with 500  $\mu\text{m}$  thick panels and three entirely controlled systems in low LEO. 70
- Figure 5.6 Comparison between the displacements and the masses of the systems in the stiffened case with 200  $\mu\text{m}$  and 500  $\mu\text{m}$  thick panels and three entirely controlled systems in high LEO. 70
- Figure 5.7 Comparison between the control torques and the masses of the systems in the stiffened case with 500  $\mu\text{m}$  thick panels and three entirely controlled systems in low LEO with inertial attitude. 71
- Figure 5.8 Comparison between the control torques and the masses of the systems in the stiffened case with 200  $\mu\text{m}$  and 500  $\mu\text{m}$  thick panels and three entirely controlled systems in high LEO with inertial attitude. 71
- Figure 6.1 An example of piezo-film, from [www.meas-spec.com](http://www.meas-spec.com). 74
- Figure 6.2 Working principle of dielectric elastomers. 75

# LIST OF TABLES

Table 1.1	Relative temperature coefficients of a set of thin-film modules and of a traditional c-Si wafer-based module for comparison. Tested under AM1.5 conditions. [24]	9
Table 2.1	Young's modulus, Poisson's ratio and density of Kapton®.	13
Table 2.2	Stiffness and damping factors of different thicknesses layer ( $L = 5.39$ m).	14
Table 2.3	Resonance frequencies of the orbits at different heights and corresponding lengths of a $25 \mu\text{m}$ layer.	18
Table 2.4	Masses in kilograms of the different configurations (CF <sub>1</sub> has a 5.39 m long panel, CF <sub>2</sub> corresponds to a 5.67 m panel).	19
Table 2.5	Instantaneous power production of an ideal panel.	20
Table 2.6	Atmospheric densities with mean solar activity. * is an estimated value.	23
Table 3.1	Results of the simulations at 300 km altitude with inertial attitude.	34
Table 3.2	Results of the simulations at 300 km altitude with nadir-pointing attitude with the satellite inclined by $45^\circ$ . In this table the maximum values collected during the first 1000 seconds are reported.	34
Table 3.3	Results of the simulations at 750 km altitude with inertial attitude.	35
Table 3.4	Results of the simulations at 750 km altitude with nadir pointing attitude.	36
Table 3.5	Results of the simulations at 1000 km altitude with inertial attitude.	36
Table 3.6	Results of the simulations at 1000 km altitude with nadir pointing attitude.	36
Table 4.1	Authority of the control system of the panels in low LEO.	47

Table 4.2	Results of the simulations at 300 km altitude with inertial attitude. 48
Table 4.3	Results of the simulations at 300 km altitude with nadir pointing attitude. 48
Table 4.4	Authority of the control system of the panels in high LEO. 49
Table 4.5	Results of the simulations at 750 km altitude with inertial attitude. 50
Table 4.6	Results of the simulations at 750 km altitude with nadir pointing attitude. 50
Table 5.1	Difference between the masses (in kg) of the different stiffened configurations (in CF1 the panel length is 5.39 m, in CF2 it corresponds to 5.67 m) and the 25 $\mu$ m thick panels. In the last column, the percentage difference is reported. 69

# NOMENCLATURE

$\delta x_L$	Displacement of the left panel tip
$\delta x_R$	Displacement of the right panel tip
$\eta$	Efficiency
$\hat{v}_s$	Unit vector corresponding to $\vec{v}_s$
$\mu$	Earth's gravitational constant
$\nu$	Poisson's ratio
$\omega$	Angular velocity
$\omega_{\text{orb}}$	Orbital angular velocity
$\rho$	Density
$\rho_{\text{atm}}$	Atmospheric density
$\theta$	Angular displacement
$\vec{a}_{\text{cb}}$	Gravitational acceleration on the central body
$\vec{a}_{\text{panel}}$	Gravitational acceleration on the panel
$\vec{B}$	Magnetic field vector
$\vec{F}_{\text{drag}}$	Drag force
$\vec{F}_{\text{rp}}$	Force due to solar radiation
$\vec{F}_{g,\text{panel}}$	Gravity gradient force
$\vec{m}$	Residual magnetic dipole of the panel
$\vec{v}_s$	Sum of the satellite velocity and the atmospheric velocity
$\xi$	Damping ratio
$A$	Surface area
$a$	Panel width

$A_{\odot}$	Projection of the surface of the panel on the perpendicular plane with respect to the Sun vector
$c$	Damping coefficient
$c_D$	Drag coefficient
$C_R$	Reflection factor
$E$	Young's modulus
$G$	Shear modulus
$h$	Orbit altitude
$I$	Moment of inertia of a cube
$I_{yy}$	Moment of inertia about Y axis
$J_p$	Polar moment of inertia
$J_s$	Solar constant
$K_d$	Derivative gain
$K_p$	Proportional gain
$k_y$	Stiffness coefficient about Y axis
$k_z$	Stiffness coefficient about Z axis
$L$	Total length of the panel
$l$	Side length of the central body
$l_p$	Length of the i-th portion of panel
$m$	Mass of the central body
$m_p$	Mass of the i-th portion of panel
$m_d$	Terrestrial magnetic dipole
$N$	Filter coefficient
$P$	Power production
$P_{\text{rad}}$	Solar pressure
$Q$	Quality factor
$R$	Radius of the orbit

$s$	Panel thickness
$T$	Torque
$t$	Time
$T_c$	Y component of the torque necessary to control the central body
$T_{pcL}$	Torque exerted by the control system on the connecting joint between the central body and the left panel
$T_{pcR}$	Torque exerted by the control system on the connecting joint between the central body and the right panel
$T_{pL}$	Y component of the torque transmitted from the left panel to the satellite
$T_{pR}$	Y component of the torques transmitted from the right panel to the satellite
CF1	Configuration with a 5.39 m long panel
CF2	Configuration with a 5.67 m long panel
CS	coordinate system
DOF	Degree of freedom
EAP	Electro-active polymer
FITS	Fold Integrated Thin Film Stiffener
GEO	Geosynchronous Earth Orbit
LEO	Low Earth Orbit
PD	Proportional-derivative
SBSP	space-based solar power
SMA	Shape Memory Alloy
TCO	transparent conductive oxide
UV	ultraviolet



# 1 | INTRODUCTION

Future spacecraft electronics are going to be always more miniaturized in their circuitry, sensors and actuators. The traditional power subsystems based on solar energy conversion contribute considerably to the spacecraft's weight, volume and cost and are not easily miniaturized. Typically, weight and volume reductions in a spacecraft mean better performances and sometimes they represent the enabling step for the feasibility of a given mission.

Because of the harsh environment in which a satellite orbits, solar cells must have the following properties:

- high efficiency, low weight and low specific volume to minimize cells total area and mass, and to reduce costs of both manufacturing and materials;
- mechanical reliability at both low and high temperatures as the satellite works in very different conditions and performs many extreme temperature cycles during periodic eclipses;
- the capacity to withstand vibrations and severe mechanical stresses, in particular during launch;
- good tolerance to radiation damage caused by charged particles in space, especially in the natural radiation belts around Earth;
- tolerance to intense UV radiation and to degradation due to atomic oxygen;
- the capability to dissipate heat through radiation in the infrared band, as conversion efficiency decreases with temperature.

The success of a satellite mission depends significantly on the power supplied by the cells, and a high reliability is essential because on-orbit repairs or substitutions are difficult or more often impossible. As the overall satellite expenses are always very high, high reliability becomes more important than cells cost [1].

Although Si and GaAs photovoltaic technologies continue to play a key role in space, there are two areas in which improvement is required: power to mass ratio (specific power) and radiation hardness. Both of the baseline materials suffer in this regard because they are based upon bulk materials. Solar cells based on thin-film materials offer the promise of much higher specific power and much lower cost [2].

Because of array size limitations, small satellites with low power requirements ( $< 5$  kW) will possibly benefit most from thin-film technology. Nevertheless, if the array size limitations are relaxed in the future or efficiency improves, higher-power satellites may become compatible with thin-film technology as well [3].

## 1.1 BACKGROUND

Thin-film solar cells technology has been studied since the 1960s, the years in which communication satellites were rapidly evolving. These satellites needed increasingly more power supply and consequently bigger and heavier solar arrays compared to the first spacecrafts, which required only some hundred watts of power. In those years, thin-film cells such as CdS on  $\text{CuS}_2$  heterojunction devices were developed to tackle the mass issue, but unfortunately this technology was not considered for future launches because of its severe degradation over time. For the next thirty years, silicon wafer-based solar cells were extensively used for space applications because of their better performances and stability [4]. In the 1980s there was the advent of GaAs solar cells, which had higher efficiency and radiation hardness than Si-cells, but 6–9 times their manufacturing costs [1].

Afterwards, during the 1990s, while GaAs modules were beginning to be used in space applications (for example on the Iridium constellation), thin-film technology based on inorganic materials was having a rapid development, both in laboratory and in industry. Thin-film arrays were used on the Hubble Space Telescope in a flexible roll-out configuration. The active material was deposited on a flexible polyimide blanket. The two array wings were deployed by a tubular, extensible boom deployment system. These two solar arrays were substituted during Servicing Mission 1 in December 1993 owing to degradation and to reduce the mechanical vibrations caused by ex-

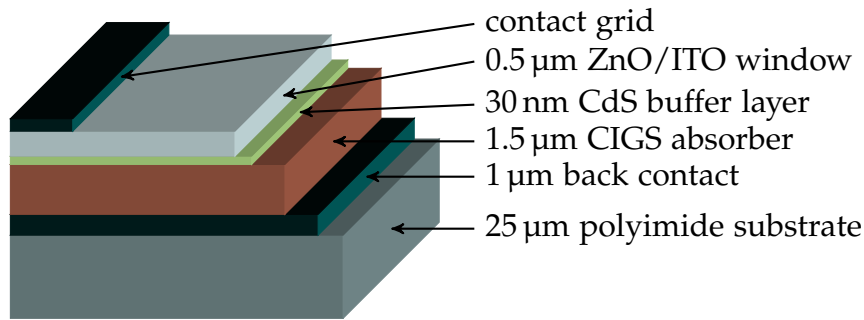


Figure 1.1: Schematic drawing of a flexible CIGS TFSC. Not to scale. [2]

cessive flexing of the solar panels during the telescope's orbital transition from cold darkness into warm daylight with rigid and more reliable silicon solar panels [4].

Samples of thin cells and arrays have flown for the first time in 1987 on LIPS III mission [5]. Other experiments have flown in PASP-Plus in 1994 [6] and on the AFRL Roadrunner mission in 2006 [7, 8].

## 1.2 SOLAR CELLS LAYOUT

Thin-film solar cells consist of several layers of different materials, with thicknesses as low as a few nanometers. The characteristic physical and chemical properties of each layer influence the overall behavior and performance of the cell. In general each cell consist of a substrate, a transparent conductive oxide (TCO) contact, a window layer (p or n-type), an absorber layer (i or p-type) and a metal contact layer as shown in figure 1.1 [9]. The active layer of the cell consists of materials of different nature: the two most important classes are briefly presented in the paragraphs below.

### 1.2.1 Inorganic materials

Inorganic thin-film cells have obtained a rapid progress in the last decades and this technology has achieved a sufficient maturity to be exported to terrestrial market, currently largely dominated by silicon-based PV technology with a worldwide share of more than 94 % in 2007 [10].

In particular, copper indium gallium diselenide (CIGS), cadmium telluride (CdTe) and amorphous silicon (a-Si) appear to have a good chance to meet the several requirements essential for panels to be used in space environment [4].

One important issue of this class of cells with respect to the silicon wafer-based is that good small-area cell efficiencies has not easily translated to array efficiencies. While the best Si module efficiencies are on the order of 92 % of cell efficiencies, CIGS modules are usually only a little over 70 % and CdTe is approximately 65 % [11].

### 1.2.2 Polymer materials

Polymer solar cells are a relatively new technology, which is currently being actively researched. They present numerous advantages, such as low material consumption resulting from high absorption coefficient, large availability, low manufacturing energy requirements and costs. Other advantages include mechanical flexibility, low specific weight, tunable material properties and high transparency. On the other hand, their principal drawbacks are their still low conversion efficiency, which reached 10.6 % in 2012 on tandem cells, and their poor stability [12]. Furthermore, it is known that for this cells space qualification costs are significant and their behavior under radiation and other space conditions has not been well established yet [11].

## 1.3 THE SUBSTRATE

The substrate is a passive component, required to be mechanically stable, inert during fabrication and with a thermal expansion coefficient similar to that of the other deposited layers in order to avoid peeling-off issues [9].

At the beginning, thin film cells were developed on rigid soda lime glass substrates, which lead to higher efficiencies with respect to cells deposited on flexible foils, but they are substantially useless on satellites since they lose their potential mass reduction. Nevertheless, this rigid substrate remains interesting for terrestrial applications. On the other hand, flexible substrates are commonly made of metal or polymer foils [3]. Power conversion efficiencies achieved on metal foils such as

titanium or stainless steel are slightly higher with respect to polymer foils, but the latter gives the possibility of a monolithically interconnected panel. On the other hand, taking into account the need to use space qualified materials, Kapton® H and HN from DuPont, and Upilex®-S from UBE are possible choices as polyimide substrates [13]. In the following chapters, simulations are based on Kapton® HN substrates.

## 1.4 COST BENEFITS OF THIN-FILM TECHNOLOGY

Thin-film technology provides several advantages through reduction in both manufacturing and launch expenses.

Manufacturing costs are a considerable voice in the production of a spacecraft. For a medium-sized satellite providing 5 kW the estimated expense just for the array manufacturing can exceed two million dollars, while with a thin-film technology the cost would be reduced to less than \$ 500,000.

Another important benefit offered by thin-film technology is the overall mass reduction in the power system which typically takes up to a quarter of the total mass budget. This is due to the fact that the most of the single crystal cells (for example Silicon and GaAs cells) are necessarily heavy because the substrate in which the active part of the cell lies must be made as a single crystal as well. This implies that substrates must be thick to be mechanically strong enough to survive the launch and the space environment. In particular, a typical single-crystal silicon solar array with its support structure takes about a third of the power system mass. A typical cell may weight more than  $1 \text{ kg/m}^2$ , while a thin-film solar cell can reach  $0.1 \text{ kg/m}^2$  and even if the latter are less efficient they could provide considerable launch cost savings, which can be estimated to be an order of magnitude less then the traditional technology [14].

According to [15] and [16], the cost breakpoint for thin-film arrays occurs when efficiency is more than 12.6%. A further increase of the efficiency would not bring a substantial benefit in terms of costs, but would allow a reduction in surface area, hence a minor expense in terms of control system.

## 1.5 PERFORMANCES

### 1.5.1 Efficiency

Future missions will need much higher specific power from the solar array, and therefore higher efficiencies from the photovoltaic blanket than even the optimized amorphous silicon cells can provide.

In 2013, scientists at Empa, the Swiss Federal Laboratories for Materials Science and Technology, developed terrestrial CIGS cells on flexible polymer foils with a new record AM1.5<sup>1</sup> efficiency of 20.8 % for converting sunlight into electricity [17]. Figure 1.2 shows the up-to-date trend in AM1.5 efficiency of various types of solar cells gathered by NREL Laboratories. Green lines report thin-film technology efficiency trend. Space efficiency is typically 2–3 absolute percentages above terrestrial efficiency, and the translation between the two global standard conditions has to be performed through ASTM E-490-2000.

### 1.5.2 Radiation resistance

In addition to cost and weight savings for the overall mission, thin-film solar cells are definitely more radiation-resistant with respect to single-crystal cells. This is an important characteristic for devices designed for being used in the radiation-rich space environment and this can possibly extend mission lifetimes.

On this regard, many experiments have been done under high energy electron and proton irradiation [18–21].

Under certain radiation conditions thin-film cells show even a slightly better performance after irradiation.

Single-crystal silicon cells which perform a beginning-of-life AM0<sup>2</sup> efficiency of about 18 % degrade to 13.1 % after exposure to  $10^{15}$  electrons/cm<sup>2</sup> of 1 MeV electrons. GaAs cells show similarly significant performance degradation. By contrast, they found on CIS (copper indium diselenide) solar cells a much better behavior, demonstrating that initially greater-than-10 % efficient cells retained more than 85 % of their performance after exposure to more than  $3 \times 10^{16}$  protons/cm<sup>2</sup> at 10 MeV, a ra-

<sup>1</sup> AM1.5 means 1.5 atmosphere thickness, corresponds to a solar zenith angle of  $z = 48.2^\circ$ , commonly used for mid-latitude nations.

<sup>2</sup> The spectrum outside the atmosphere, the 5800 K black body, is referred to as “AM0”, meaning “zero atmospheres”. Solar cells used for space power applications are generally characterized using AM0.



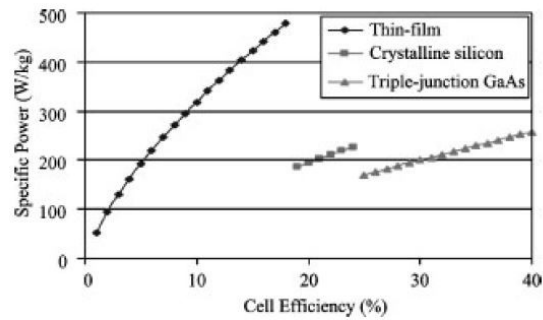


Figure 1.3: Specific power of lightweight solar array with thin-film, thin crystalline silicon and crystalline GaAs solar cells as a function of conversion efficiency. [23]

diation exposure typical of intermediate circular and medium altitude Earth orbits [3].

### 1.5.3 Specific power

Thin-film solar cells became very attractive for space applications because of their high specific power, due to an important mass reduction with respect to typical crystalline solar cells. It is estimated that the specific power is increased by an order of magnitude, from the current level of 65 W/kg [22].

As it is shown in figure 1.3 the maximum specific power achievable with crystalline solar cell technology is about 200 W/kg, while thin-film solar cells with a 15–18% range efficiency have an array specific power that exceeds 400 W/kg [4].

### 1.5.4 Temperature coefficient

Thin-film panels used for space applications are subjected to extreme temperature variations, when in light or shade conditions. Generally this type of cells presents a linear dependence between conversion efficiency and increase of temperature (see table 1.1 for a comparison between some tested materials) [23].

At least for the single-junction devices, there is a possible correlation between the magnitude of the power temperature coefficient and the band gap of the corresponding absorber material, which vary from 1.1 eV for crystalline silicon, to approximately 1.8 eV for amorphous silicon ( $\sim 1.2$  eV for CIGS and  $\sim 1.44$  eV for CdTe) [24].

material	$P_{\max}$ [%/°C]
a-si (SJ)	-0.13
CdTe	-0.21
CIGS	-0.36
<b>c-Si (wafer-based)</b>	<b>-0.45</b>

**Table 1.1:** Relative temperature coefficients of a set of thin-film modules and of a traditional c-Si wafer-based module for comparison. Tested under AM1.5 conditions. [24]

## 1.6 MOTIVATIONS

Future satellites are expected to be more and more accurate in pointing capabilities, and able to perform fast and precise maneuvers in the space environment, with all its disturbances and uncertainties.

In a typical modern satellite, large flexible appendages such as solar panels wings, booms or antennas, could have an important influence on the vehicle attitude by possibly degrading the control performances. Such a mechanical system is subjected to nonlinear dynamics which include rigid and flexible mode interaction. These modes of vibrations should be expected for example during satellite maneuvers, such as slewing, rendezvous and docking and when the satellite is subjected to external perturbations, which include for example solar wind, atmospheric drag, etc. In a satellite equipped with reaction or momentum wheels, a slight misalignment can create resonance between the wheels and, for example, the solar panels, taking the satellite to possibly lose its control [25].

Thin-film solar arrays are inherently very flexible, since their cross section is typically just a few tens of micrometers. As a consequence, these structures have very low first natural frequencies. These low fundamental frequencies do not meet the requirements imposed on conventional designs.

Structures with low fundamental frequencies are also predisposed to have low buckling and crippling strength. Deployed thin-film solar arrays have to be structurally stable against all on-orbit inertia loads. However, minor buckling of the blanket itself is allowed, while buckling of possible integral stiffeners takes to dramatic issues to the performance of the solar array.

Traditional methods for the array design require a boom or a structure to keep a tension the array in order to meet a particular natural frequency requirement. This approach involves com-

plex and heavy mechanisms to deploy the blanket and forces to maintain a constant tension throughout the mission. Another approach makes use of FITS Technology, which were used in Z-folded solar arrays, on stainless steel substrate [26]. Also a tethered inflatable geodetic sphere populated with large area solar cells was proposed for small satellites [27].

In this work, the solar cells are thought to be deposited on polyimide blankets, which are lighter than metal substrates and permit rolled configurations. This leads to even more mass savings and less complex deployment systems, that are very important in small satellites.

Over the last years space systems miniaturization has been sought in order to reduce mission costs and, therefore, interest grew in the development of microsatellites and nanosatellites for low Earth orbits (LEO). This technology requires the capability of collecting enough power for onboard instruments with a low weight and volume spacecraft. Body-mounted solar cells are unable of providing enough power because the overall surface area of the satellite is too small.

However, the system studied in this work can be easily applied to any orbital height changing the entity of the disturbances. For example, the system can be analyzed in Geosynchronous Earth Orbits (GEO), considering that the only disturbance that should be taken into account in a static condition is solar radiation pressure. Typically, very large satellites are used in GEO orbits, requiring a large amount of power, that translates into very large power systems. It is possible that in future years, as the technology improves, the overall dimension of the system will become smaller with respect to the current very large satellites. This suggests that the dimension of the stowed panels should be reduced. Therefore, thin-film technology have a chance to achieve an important role also in GEO orbits.

Additional studies could also be addressed to space-based solar power (SBSP) systems, which are a new concept of satellites provided with very large solar blankets placed on Earth orbit. These systems are currently under development by many companies and space agencies (e.g. EADS Astrium and JAXA [28]) and are thought to collect electricity on space and transmit it to Earth stations through a wireless energy transmission.

# 2 | MODEL DEFINITION

In this chapter the model on which the numerical simulations are executed is described as well as all the simplifying assumptions adopted.

## 2.1 GEOMETRY AND MATERIAL

The simulated spacecraft consists of a central rigid body, cubic shaped with a different distribution of the masses along the three axes of symmetry. Two large and flexible solar panels are connected to the main central body. The dimensions of the solar arrays are chosen considering the altitude of the orbit as explained later. Consequently, the increase of the dimension of the wings takes to a higher power production.

Thin-film solar cells are composed by a number of different layers (see figure 1.1), among which the substrate where the active layers are deposited is the thicker. In particular, a typical thickness of the substrate in solar cells deposited on a polyimide material is  $25\ \mu\text{m}$  while the sum of the thicknesses of the other layers is less than  $5\ \mu\text{m}$ . For this reason, mechanical properties of flexible solar arrays are assumed to coincide with those of the chosen substrate. The properties of Kapton® HN are used in the simulations.

The size of the central body is assumed to be small, since mass savings due to flexible panels are more significant on a small satellite. Simulations are executed on satellites in which weight ranges between 5 kg and 50 kg.

## 2.2 MODEL DESCRIPTION

The model has been developed using *Matlab® SimMechanics™*, which provides a multi-body simulation environment for 3D mechanical systems, mainly used in robotics. The multi-body system under study is modeled through a number of blocks which correspond to bodies, joints, constraints, and force

elements. The software formulates and solves the equations of motion of the complete mechanical system. In addition, an automatically generated 3D animation allows the user to visualize the system dynamics, either through the equivalent inertia ellipsoids or importing the geometry from a CAD model.

### 2.2.1 Satellite orientation

The software automatically sets up a single absolute inertial reference frame and coordinate system (CS) called *World*. Each mass has its own *Body* coordinate frame, fixed on the system's rigid bodies and moving rigidly with them.

In order to define the disturbances that act on the satellite in the easiest possible way, the *World* CS coincides with the *Orbital* frame for the considered spacecraft, where the X axis is perpendicular to the panels, the Y axis lays along the width of the panels and the Z axis lays along their length.

The simulations are performed in two different attitude configurations:

- *inertial-pointing attitude*: the axes of the *Body* coordinate system of the central rigid body are always parallel to the inertial coordinate system centered on the Earth, with the X axis pointing the Vernal point, Z axis pointing the North Pole and the Y axis to complete the right-handed CS;
- *nadir-pointing attitude*: the X axis of the *World/Orbital* coordinate system of the central body of the satellite points always to the center of the Earth in the negative direction, Z points to the flight direction and the Y axis completes the frame. The simulations are performed on a satellite inclined by  $45^\circ$  with respect to Y *World* axis.

### 2.2.2 Masses

The flexible components were arbitrarily discretized in eight rigid masses, each with its proper material and geometric characteristics. The central body is considered as a single rigid mass. The mass of the central body is arbitrarily fixed, between 5 kg and 50 kg.

The material properties of the flexible components are those of Kapton®, listed in table 2.1. The elastic behavior of the material is considered to be linear since the strain levels are expected

to be low in the simulations. The viscous properties of the material are considered including an equivalent linear damping coefficient to the material model.

$E$ [Pa]	$\nu$	$\rho$ [kg/m <sup>3</sup> ]
2.5 E9	0.34	1420

**Table 2.1:** Young's modulus, Poisson's ratio and density of Kapton®.

In SimMechanics™ environment, it is necessary to provide to each body the mass and the tensor of inertia of each single mass, with respect to the *Body* CS.

### 2.2.3 Joints

Each mass is connected to the adjacent through a joint. With regard to the panels, only two rotational degrees of freedom are assumed to be free: one along the width (bending) and one along the length of the panel (torsion). The blocked degree of freedom is the one along the axis perpendicular to the panel, since its stiffness coefficient is much higher than the others. The stiffness coefficients between two masses are calculated through the equations (2.2) and (2.3).

$$k_y = 3 \frac{EI_{yy}}{l_p^3} \quad (2.1)$$

where  $I_{yy}$  is the moment of inertia:

$$I_{yy} = \frac{as^3}{12} \quad (2.2)$$

while:

$$k_z = \frac{J_p G}{l_p} \quad (2.3)$$

where  $k_y$  is the bending stiffness while  $k_z$  is the torsional stiffness,  $a$  is the width of the panel while  $s$  is its thickness,  $l_p$  is the length of the portion of the panel associated to a single mass,  $G$  is the shear modulus, calculated through the equation:

$$G = \frac{E}{2(1+\nu)} \quad (2.4)$$

and  $J_p$  is the polar moment of inertia, which is:

$$J_p = \frac{as}{12}(a^2 + s^2). \quad (2.5)$$

The damping coefficient is calculated through equation (2.6), which is valid for both the axes, each with its stiffness coefficient:

$$c = 2\xi\sqrt{km_p} \quad (2.6)$$

where  $m_p$  is the mass of the portion of the panel considered and  $\xi$  is the damping ratio, calculated through the quality factor  $Q$  assumed to be 40 for Kapton® (poor damping capacity):

$$\xi = \frac{1}{2Q} \quad (2.7)$$

The model is described through the lumped mass method, with the bodies connected together through a parallel system of damped linear oscillators, equivalent to a torsional spring and damper for each joint. The torque  $T$  between the bodies is a function of the relative angular displacement  $\theta$  and the angular velocity  $\omega$  of the bodies, given by

$$T = -k(\theta - \theta_0) - c\omega. \quad (2.8)$$

The parameters  $\theta_0$ ,  $k$ , and  $c$  represent the spring offset, spring constant, and damper constant, respectively. The spring offset is set to zero. The coefficients  $k_y$  and  $k_z$  are related to the elastic behavior of the material, while  $c_y$  and  $c_z$  represent its damping capability.

For the considered material, the stiffness and damping factors for some Kapton® layers of different thicknesses are listed in table 2.2.

The center of mass of the satellite is coincident and connected to a rotational joint with three degrees of freedom. This joint

$s$ [ $\mu\text{m}$ ]	$k_y$ [N/m]	$k_z$ [N/m]	$c_y$ [Ns/m]	$c_z$ [Ns/m]
25	1.2772 E-5	184.61	8.739 E-6	0.033
100	8.1742 E-4	738.42	1.398 E-4	0.133
200	6.5393 E-3	1476.85	5.593 E-4	0.266
500	0.1022	3692.12	3.496 E-3	0.665

**Table 2.2:** Stiffness and damping factors of different thicknesses layer ( $L = 5.39$  m).

is connected to the *ground* block, which connects the joint to a fixed location in the *World* coordinate system. Therefore, the satellite can freely rotate about the three coordinate axes.

An example of a joint is presented in figure 2.1. The block on the center defines the two rotational degrees of freedom, and it is linked through the upper connection lines with the adjacent masses, called *base* (B) and *follower* (F). Their sequence together with axis direction indicate the sign of forward motion. The Joint Initial Conditions are set to zero for each axis, so that the panel is initially straight deployed. A joint sensor for each degree of freedom measures the instantaneous angular position and angular velocity, which are multiplied respectively by the stiffness and the damping coefficient. The joint actuator receives the input in terms of torque and exerts it on the central block. Lastly, the PD Controller block on the right adds its contribution in terms of torque on the bending degree of freedom.

Inertial and nadir-pointing attitudes are achieved with an ideal actuator placed at the center of mass of the central body, such as for example a set of reaction wheels, which ideally keeps the satellite always pointing the instantaneous correct direction. It is possible to find the ideal amount of control torque which has to be exerted from the reaction wheels to maintain the desired attitude through a body sensor connected with the three DOF joint located on the center of mass of the satellite. The model of the satellite performing inertial attitude is shown in figure 2.2. The joint actuator forces the central body to rotate around Y axis with orbital velocity. The Initial Conditions are set to zero.

#### 2.2.4 Dimensions of the panels

The dimensions of the panels have been selected so that the first resonance frequency of the 25  $\mu\text{m}$  thick panel coincides with the orbital frequency, in order to have the panels the most excited possible at every orbit height. The used equation is linear but is still valid even for a highly flexible foil in the case of small strains.

The width  $a$  of the panels has been chosen arbitrarily to be 0.4 m, a dimension which is less than the side of the modeled central body, in order to avoid all the possible problems connected with deployment. In this way it is possible to consider the panels as simple roll-up foils. If the panels were wider,

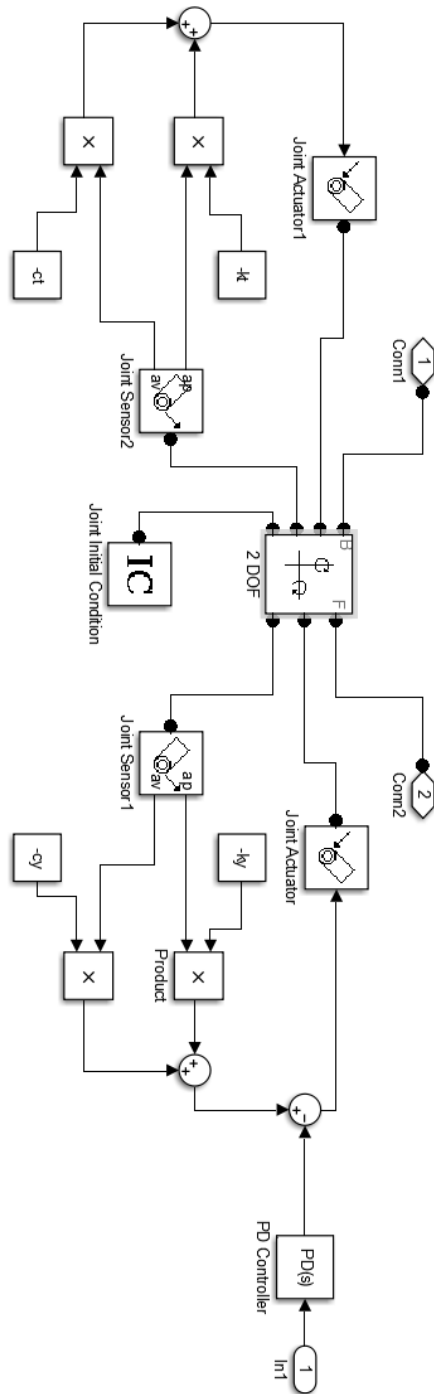


Figure 2.1: Example of a joint subsystem.

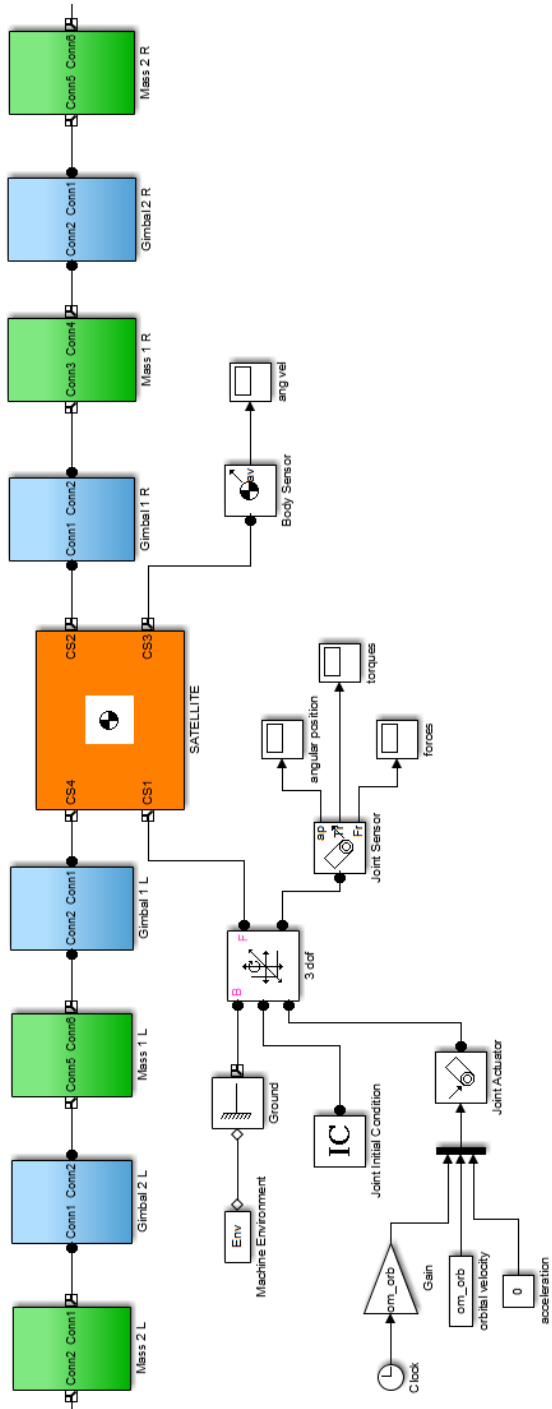


Figure 2.2: The central body (orange) is connected through the joints (light blue) with the panels (green).

$h$ [km]	$\omega_{\text{orb}}$ [rad/s]	$f_{\text{orb}}$ [Hz]	$L$ [m]
300	1.1569 E-3	1.8413 E-4	5.39
500	1.1068 E-3	1.7616 E-4	5.51
750	1.0491 E-3	1.6097 E-4	5.67
1000	9.9623 E-4	1.5856 E-4	5.81

**Table 2.3:** Resonance frequencies of the orbits at different heights and corresponding lengths of a 25  $\mu\text{m}$  layer.

it would be necessary to fold them up and provide the panel a more complicated mechanism to be deployed. Furthermore, a long and less wide panel reaches lower natural frequencies, and it can enter resonance more easily with all the orbit disturbances.

The equation used to calculate the first resonance frequency of the panel thought as a cantilever beam is the following:

$$\omega_{\text{panel}} = \frac{1.875^2}{L^2} \sqrt{\frac{Es^2}{12\rho}} \quad (2.9)$$

where  $L$  is the total length of the panel,  $E$  is the Young modulus,  $s$  is the thickness and  $\rho$  is the density of the material.

From orbital mechanics, the frequency of an orbit is:

$$\omega_{\text{orb}} = \frac{2\pi}{T} \quad (2.10)$$

where  $T$  is the period of the orbit. In order to calculate the length of the panel which has the first resonance frequency coincident with  $\omega_{\text{orb}}$ , the equation is:

$$L = \sqrt{\frac{1.875^2}{\omega_{\text{orb}}} \sqrt{\frac{Es^2}{12\rho}}} \quad (2.11)$$

The resonance frequencies of each considered orbit altitude and the relative panel lengths are reported in table 2.3.

The values have been verified with a finite elements simulation with MSC software Patran®. The deformed shapes referred to the first two resonance frequencies of a 5.51 m long panel are shown in figure 2.3 and 2.4.

Considering that mass reduction on a small satellite is a great issue, the mass of the power system should be the smallest possible. In table 2.4 the masses of the panels of the four configurations are reported.

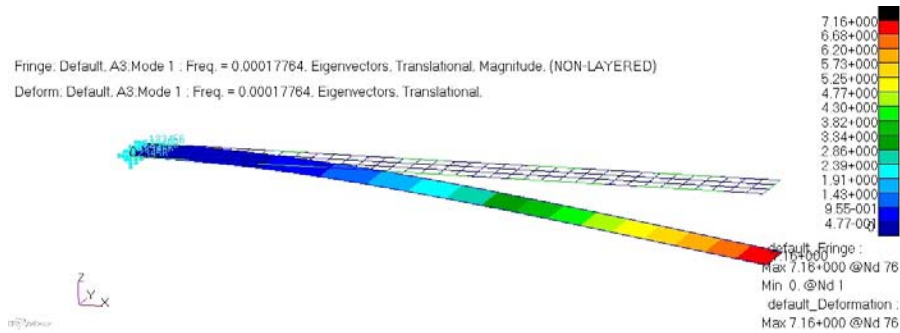


Figure 2.3: First natural frequency of a 5.51 m long panel.

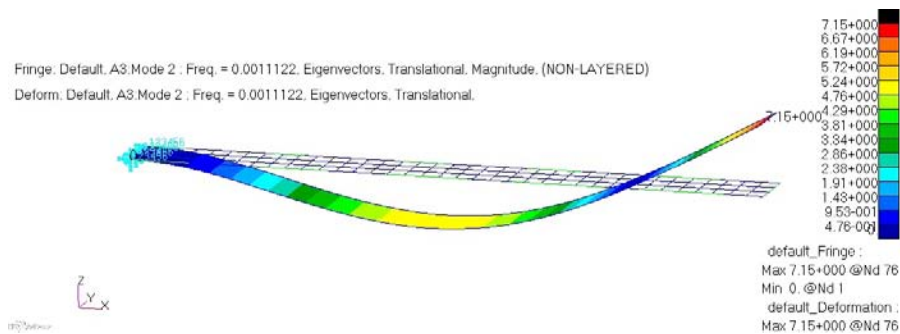


Figure 2.4: Second natural frequency of a 5.51 m long panel.

$s$ [ $\mu\text{m}$ ]	CF <sub>1</sub>	CF <sub>2</sub>
25	0.1531	0.1610
100	0.6123	0.6441
200	1.2246	1.2882
500	3.0615	3.2206

Table 2.4: Masses in kilograms of the different configurations (CF<sub>1</sub> has a 5.39 m long panel, CF<sub>2</sub> corresponds to a 5.67 m panel).

It is clear that the configuration which considers 500  $\mu\text{m}$  panels is about 20 times heavier than the 25  $\mu\text{m}$  one, which, however, requires a control system. Nevertheless, simulations are done in both the configurations and the collected results are compared and discussed in the following chapters.

### 2.2.5 Power production

As the principal aim of the thesis is to demonstrate the feasibility of a large power system based on solar panels on a small satellite, the power production has to be high with respect of the size of the considered satellites.

The power production can be estimated with the equation:

$$P = \eta J_s A \quad (2.12)$$

where  $\eta$  is the efficiency, that is assumed to stay in a range between 0.1 and 0.3,  $J_s$  is the solar constant in this case approximated to  $1300 \text{ W/m}^2$  and  $A$  is the surface area of the panel exposed to sunlight.

Being the width of the panel fixed to 0.4 m, the maximum instantaneous power production with the panel always facing the Sun can be estimated as shown in table 2.5. In figure 2.5 the simulated power production of the two panels is reported.

$h$ [km]	$L$ [m]	$P_{\min}$ [W]	$P_{\text{avg}}$ [W]	$P_{\max}$ [W]
300	5.39	280.28	560.56	840.84
500	5.51	286.52	573.04	859.56
750	5.67	294.84	589.68	884.52
1000	5.81	302.12	604.24	906.36

Table 2.5: Instantaneous power production of an ideal panel.

## 2.3 ORBITAL DISTURBANCES

Typically, small satellites are designed for working in low Earth orbits (LEO). The simulated orbits are circular and their altitudes are 300 km and 750 km. Four main disturbances are considered and discussed below: atmospheric drag, solar radiation pressure, gravity gradient and geomagnetic field interaction.

### 2.3.1 Drag

This disturbance, due to atmospheric viscous friction, is very important for satellites that orbit below 2000 km. Atmosphere density depends significantly on solar activity which is not very

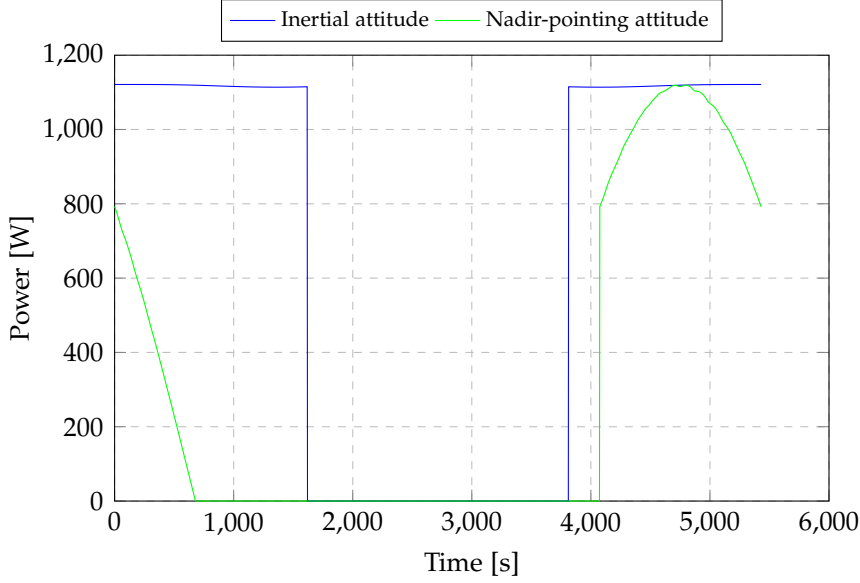


**Figure 2.5:** Instantaneous power production of the two simulated 500  $\mu\text{m}$  thick panels in the two attitude configurations at 300 km height.

predictable: for these simulations, medium solar activity has been considered. In the periods of high solar activity, the atmospheric density increases by about two orders of magnitude. Hence, satellites would be even more affected by this disturbance. The atmospheric density constant was extracted from the MSIS-E-90 model.

The drag force acts on the satellites circularizing elliptical orbits and lowering their altitude, therefore it becomes necessary to perform re-boosts to avoid deorbiting. Drag force depends strongly on orbital altitude and it is analytically expressed by the equation:

$$\vec{F}_{\text{drag}} = \frac{1}{2} c_D A \rho_{\text{atm}} |v_s|^2 \hat{v}_s \quad (2.13)$$

where  $A$  is the projection of the surface of the panel perpendicular to the direction of the velocity vector,  $c_D$  is the drag coefficient assumed to be 1 as the projection of the surface in this case is a rectangle,  $\rho_{\text{atm}}$  is the atmospheric density, the vector  $\vec{v}_s$  is the sum of the satellite velocity and the atmospheric velocity due to the winds, assumed to be null in this case for simplicity, and  $\hat{v}_s$  is the corresponding unit vector.

Figure 2.6 shows the entity of drag force on the mass at the left panel tip in case of inertial attitude at 300 km altitude.

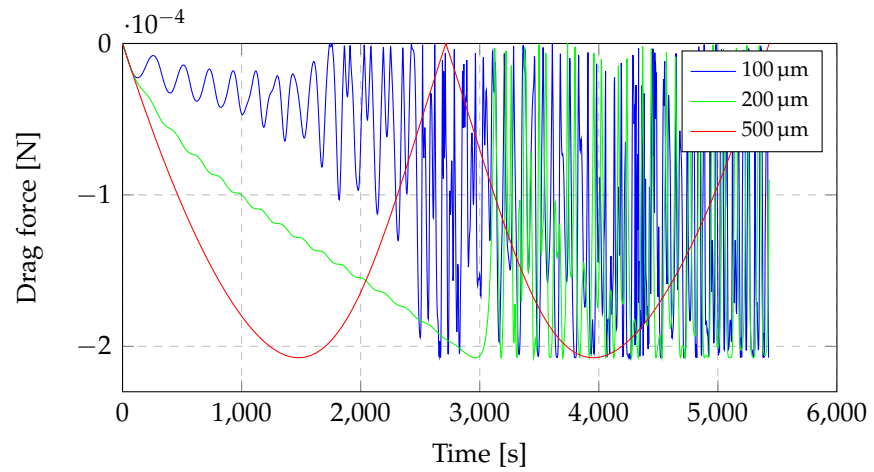


Figure 2.6: Drag force at 300 km for panels of different thicknesses.

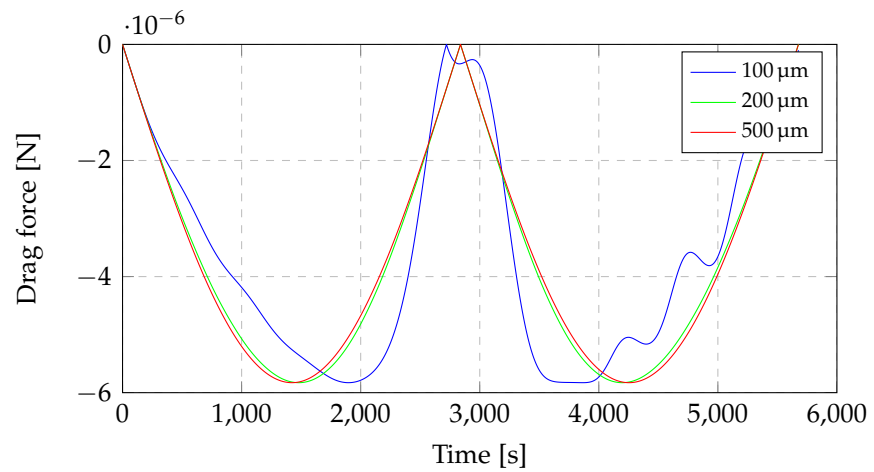


Figure 2.7: Drag force at 500 km for panels of different thicknesses.

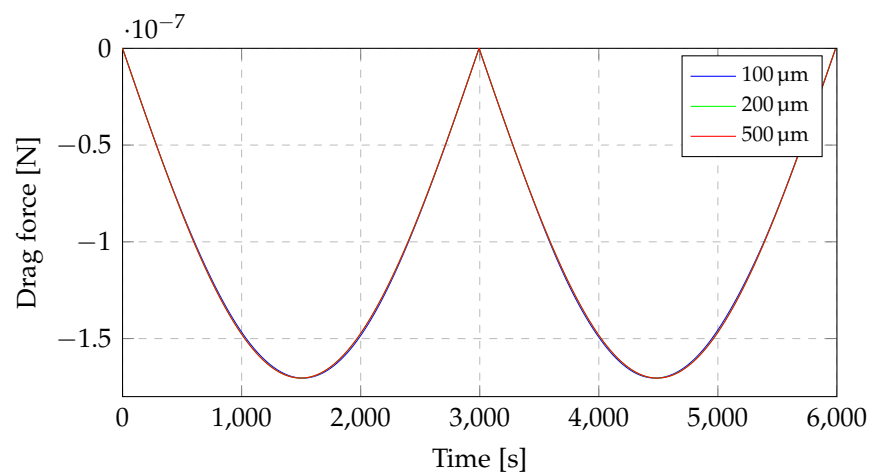


Figure 2.8: Drag force at 750 km for panels of different thicknesses.

$h$ [km]	$\rho_{\text{atm}}$ [kg/m <sup>3</sup> ]
300	2.58 E−11
500	7.30 E−13
750	2.15 E−14
1000	1.00 E−15*

**Table 2.6:** Atmospheric densities with mean solar activity. \* is an estimated value.

The maximum value is  $-2.07 \text{ E}^{-4} \text{ N}$  in  $-Z$  direction, and it is reached when the panel is perpendicular to the velocity vector. It is clear that the thinner panels are strongly affected by this disturbance. On the other hand, figure 2.7 referred to a 500 km altitude orbit shows a smaller deflection with a maximum drag force of  $-5.82 \text{ E}^{-6} \text{ N}$ . At last, the force exerted on a 750 km altitude orbit is presented in figure 2.8. The maximum force exerted at this altitude is  $-1.70 \text{ E}^{-7} \text{ N}$ .

### 2.3.2 Solar radiation pressure

Solar radiation pressure becomes a fundamental disturbance when the surface exposed to sunlight is very large. In addition to this, if the object is very flexible, its effects are not negligible. The force explicated can be easily calculated through equation (2.14):

$$F_{\text{rp}} = \nu C_{\text{R}} A_{\odot} P_{\text{rad}} \quad (2.14)$$

where  $A_{\odot}$  is the projection of the surface of the panel on the perpendicular plane with respect to the Sun vector,  $\nu$  is the shadow function, which varies between 0 (shadow) and 1 (light). For simplicity, the condition of penumbra is not considered.  $C_{\text{R}}$  is a reflection factor that is assumed 1.21 for solar panels, while  $P_{\text{rad}}$  represents the pressure exerted by the solar radiation for a satellite in Earth orbit, its value being approximately  $4.56 \text{ E}^{-6} \text{ N/m}^2$  [29].

Since the radiation pressure depends exclusively on the surface exposed to the sunlight, besides the other values which are constants, figure 2.9 reports the force exerted by the solar radiation pressure on the tip of a  $500 \mu\text{m}$  thick panel at different altitudes.

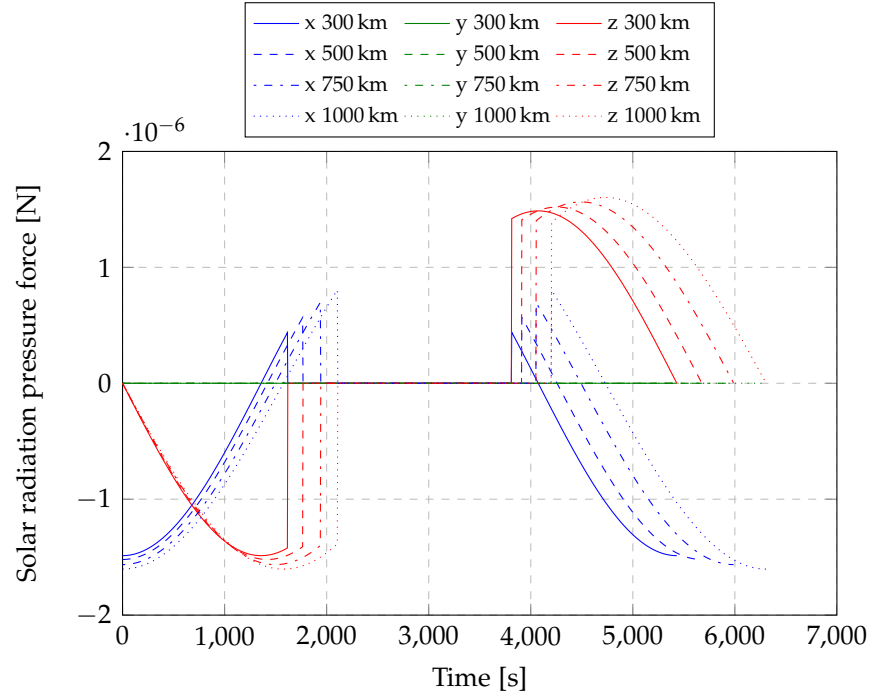


Figure 2.9: Force exerted by solar radiation pressure at different altitudes on a  $500 \mu\text{m}$  thick panel in equatorial orbit with inertial attitude, in the *World* CS.

### 2.3.3 Gravity gradient

Differently from the disturbances listed above in which the center of aerodynamic and solar pressure on the central body can be considered coincident with its center of mass and therefore the disturbances on the central body can be neglected, the gravitational gradient must be considered also on the central body if the masses are not equally distributed along the tree axis of symmetry.

The equations of the force that acts on the central body are:

$$\vec{F}_{g,cb} = \frac{3}{2} \frac{\mu}{R^3} \begin{Bmatrix} (I_y - I_z) \sin(2\phi) \cos^2(\theta) \\ (I_z - I_x) \sin(2\theta) \cos(\phi) \\ (I_x - I_y) \sin(2\theta) \sin(\phi) \end{Bmatrix} \quad (2.15)$$

where  $\mu$  is the Earth's gravitational constant,  $R$  is the radius of the orbit (constant if circular),  $I_x$ ,  $I_y$  and  $I_z$  are the principal moments of inertia of the central body,  $\phi$ ,  $\theta$  (and  $\psi$ ) are the Euler angles which can be extract from the rotation matrix of the central body with respect to the *World* coordinate system.

In these simulations,  $I_x = 0.1 \cdot I$ ,  $I_y = I$  and  $I_z = 0.9 \cdot I$  where  $I$  represents the moment of inertia of a cube:

$$I = \frac{ml^2}{6}. \quad (2.16)$$

In addition to this, the contribution of the gravitational gradient on the panels must be added. The gravitational acceleration which acts on the central body was calculated with the equation:

$$\vec{a}_{cb} = -\frac{\mu}{R^2} \hat{u}_R \quad (2.17)$$

and it was subtracted from the acceleration calculated for the panel:

$$\vec{a}_{panel} = -\frac{\mu}{(R + \delta r)^2} \hat{u}_R \quad (2.18)$$

where  $\delta r$  is the difference of coordinates of the panel tips along the radial direction with respect to the center of the Earth, and  $\hat{u}_R$  is its unit vector.

The gravity gradient force for every single portion of the panel is then obtained multiplying their mass by the difference between equations (2.17) and 2.18:

$$\vec{F}_{g,panel} = m (\vec{a}_{panel} - \vec{a}_{cb}) \quad (2.19)$$

Therefore the gravity gradient decreases with the square root of the distance between the satellite and the center of the Earth. The effect of this disturbance is that the satellite and the panels tend to align its axis of minimum moment of inertia vertically.

Then, since the force depends on the mass, for the same orbit the force exerted by gravity gradient results one order of magnitude higher for the 500  $\mu\text{m}$  thick panels with respect to the 25  $\mu\text{m}$  thick ones. An example is reported in figures 2.10 and 2.11. The modulus of the force is maximum when the panels are aligned with the local vertical.

Especially from figure 2.10, since the panel is very flexible and tends to align along the local vertical, the component of the force that acts on the panel increase when it is about to reach the vertical position, and it tends to maintain the alignment even when the central body passes the vertical. On the other side, in figure 2.11 the exerted force shows a regular trend. This

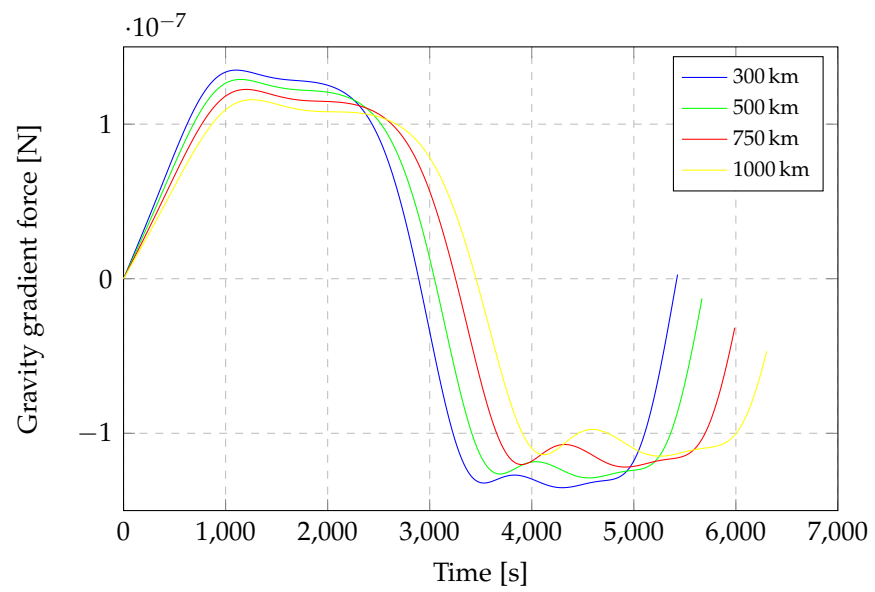


Figure 2.10: X component (along the local vertical) of the gravity gradient force at the tip of a 25 μm thick panel at different altitudes.

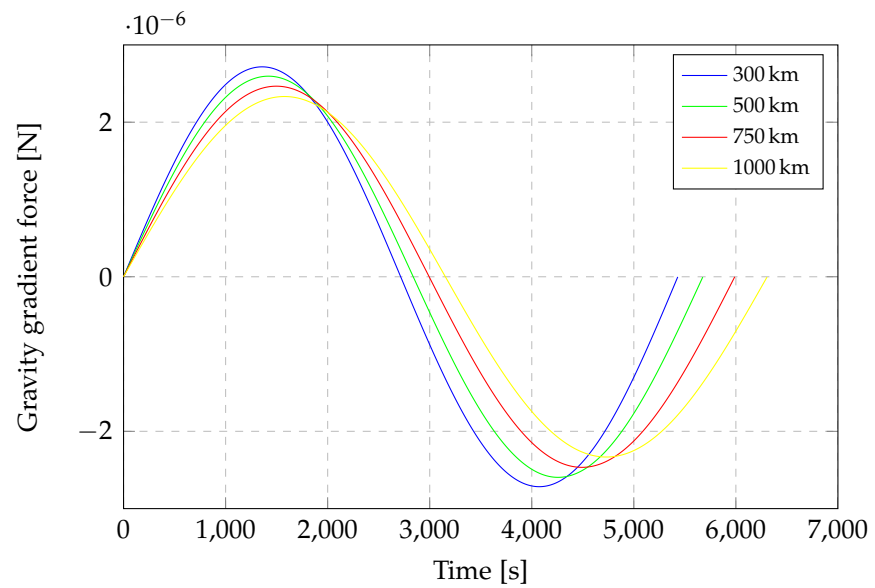


Figure 2.11: X component (along the local vertical) of the gravity gradient force at the tip of a 500 μm thick panel at different altitudes.

means that the thicker panel does not deform under its influence, while still transmitting the torque to the central body.

#### 2.3.4 Magnetic field

The Earth magnetic field generates a torque on the satellite if there is a residual magnetic dipole on it. The residual dipole on the central body is neglected in these simulations, as it is not known. In the case of thin-film panels, its vector is assumed constant along the panel, with the value of:

$$\vec{m} = \begin{Bmatrix} 10^{-4} \\ 0 \\ 0 \end{Bmatrix} \text{ A m}^2. \quad (2.20)$$

The torque exerted on the panel is given by the equation:

$$\vec{T} = \vec{m} \times \vec{B} \quad (2.21)$$

where  $\vec{B}$  is the Earth magnetic field vector. For these simulations the inclined dipole magnetic field model was used [30]. The equations for this configuration written on the orbital coordinate system are:

$$\vec{B}(r) = B_0 [3 (\hat{m}_0 \cdot \hat{r}) \hat{r} - \hat{m}_0] \quad (2.22)$$

where  $B_0$  is the constant:

$$B_0 = \frac{m}{R^3} \quad (2.23)$$

with the terrestrial magnetic dipole:

$$m_d = 7.96 \text{ E15 T m}^3. \quad (2.24)$$

If the satellite flights on polar orbits the constant  $B_0$  has to be doubled, since the magnetic field is more intense on the poles.

The unit vector on equation 2.22 is defined as:

$$\hat{r} = \begin{Bmatrix} \cos(v) \\ \sin(v) \\ 0 \end{Bmatrix} \quad (2.25)$$

where

$$v = \tilde{\omega} + \omega t \quad (2.26)$$

where  $\tilde{\omega}$  is the argument of perigee. Furthermore:

$$\hat{m}_0 = \left\{ \begin{array}{l} \sin(\theta_m) \cos(\Omega - \alpha_m) \\ -\sin(\theta_m) \cos(i) \sin(\Omega - \alpha_m) + \cos(\theta_m) \sin(i) \\ \sin(\theta_m) \sin(i) \sin(\Omega - \alpha_m) + \cos(\theta_m) \cos(i) \end{array} \right\} \quad (2.27)$$

where  $\theta_m = 168.6^\circ$ ,  $\Omega$  is the right ascension of the ascending node,  $i$  is the inclination of the orbit and  $\alpha_m$  is equal to:

$$\alpha_m = \phi_m + \Omega_E t + \alpha_{G0} \quad (2.28)$$

where  $\phi_m = 109.3^\circ$ ,  $\Omega_E$  is the rotation velocity of the Earth about its axis and  $\alpha_{G0}$  is the right ascension of Greenwich at time  $t = 0$  with respect to the Vernal point. For simplicity,  $\tilde{\omega}$ ,  $\Omega$  and  $\alpha_{G0}$  are supposed to be null. The components of the magnetic field are reported in figure 2.12 with respect to the *World* CS.

The torque exerted on the tip of the panel is reported in figure 2.13, with respect to the *Body* CS since the effect due to the magnetic field interaction is strictly connected to this reference frame. Clearly, being the only component different from zero of the residual magnetic dipole on the X direction of the *Body* CS (perpendicular to the panel), the component of the torque in this direction is null.

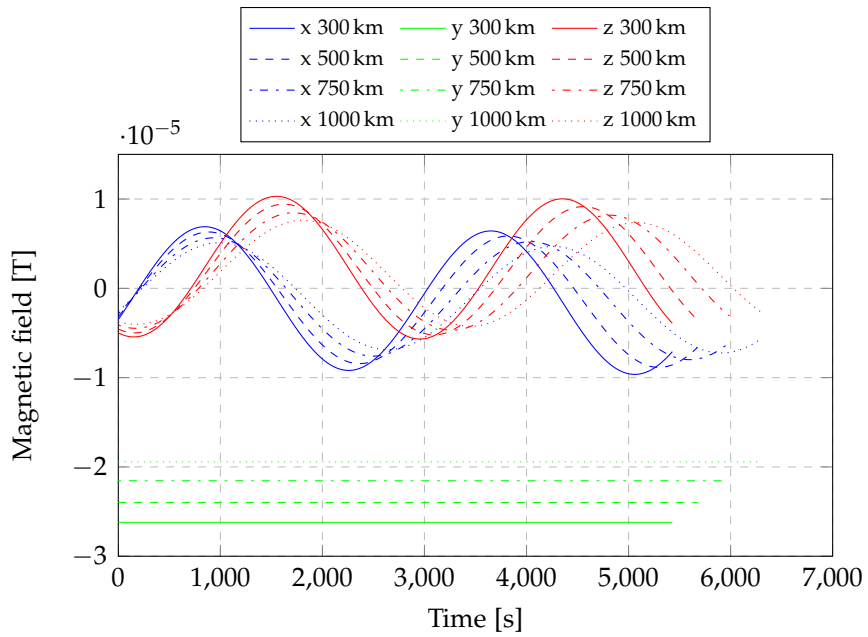


Figure 2.12: Components of the magnetic field at different altitudes.

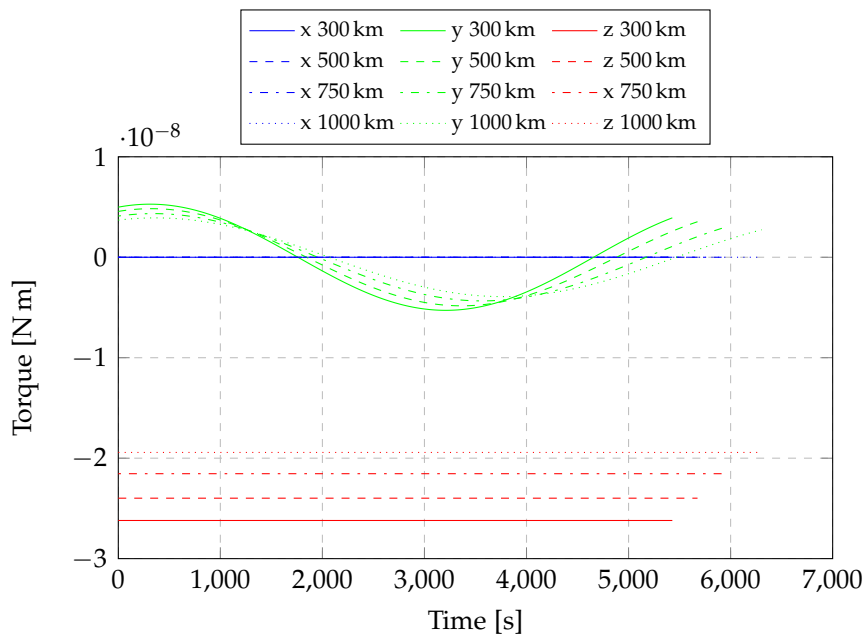


Figure 2.13: Components of the torque due to the interaction of the panels with the magnetic field at different altitudes.



# 3

## SIMULATIONS WITHOUT VIBRATIONS CONTROL SYSTEM

In this chapter the results of a number of simulations in absence of an active vibration control system are presented. The aim of these simulations is to demonstrate that a system with a 25  $\mu\text{m}$  thin Kapton® layer as substrate of the panel is not able to bear the typical disturbances present in LEO.

The disturbances are divided in two cases:

- considering only the drag resistance in low LEO;
- with the contribution of the solar radiation pressure, of the gravity gradient force and of the torque due to the interaction with the Earth's magnetic field in high LEO.

This distinction was done because the effect of the atmospheric resistance is highly dependent on the altitude. The torque transmitted from the panels to the satellite at 300 km altitude due to this disturbance is two orders of magnitude higher than the torque that would be exerted by a panel subjected exclusively to the solar radiation pressure, which is the second disturbance for relevance. Increasing the altitude, the perturbations caused by the atmospheric resistance decrease becoming negligible above 750 km, while the solar radiation pressure remains an important disturbance. At this altitude, the contribution of the torques caused by the gravity gradient on the panels are of the same order of magnitude as the torques exerted by the solar pressure. On the other hand, the torques generated by the coupling of the residual magnetic dipole of the panels with the Earth's magnetic field and transmitted to the satellite are quantitatively less relevant at every altitude. For this reason they are grouped in the second case, where the entity of the other two perturbations is lower.

The simulations were executed under a number of conditions: with inertial pointing and nadir-pointing attitude at different altitudes, varying the total surface area of the panel depending on height as explained in the previous chapter.

### 3.1 SIMULATIONS WITH 25 $\mu\text{m}$ THICK PANELS

The results of the simulations demonstrate that a panel with a 25  $\mu\text{m}$  cross section cannot stand the disturbances it is subjected to at any altitudes. The torques caused by the disturbances are sufficiently high to cause the wrapping of the panel around the central body and the collision with the other panel, making the power generation impossible. Moreover, the length of the panels was previously chosen to match the orbital frequency, therefore the solar modules are forced to enter the resonance condition.

More particularly, simulating the behavior of the system on a very low orbit (300 km) the drag force causes a torque on the panels exclusively around Y axis, while the other two axes are not affected by this disturbance. Nadir pointing simulations are performed with an inclination of  $45^\circ$  about the Y axis, because an inclination of  $0^\circ$  would not cause any deformations since the surface of the panels exposed to the drag force would be null. Nevertheless, it is important to point out that also imposing a small inclination angle to the satellite, the panels would perform an uncontrolled motion, even if in a slightly longer time. Also at 750 km altitude the panels show an uncontrolled behavior. Consequently, the simulation results obtained with SimMechanics<sup>TM</sup> become not realistic since the panels intersect and overlap. The software does not take account for overlapping of the masses, therefore it is not possible to simulate the real behavior of the system. For this reason, the model is not suitable in the case of large deformations, but it can give a qualitative idea and demonstrates when the system is not usable at all. Nevertheless, this is not a field of interest for the thesis purpose.



Figure 3.1: Behavior of 25  $\mu\text{m}$  thick panels subjected to drag force at 300 km height, at the beginning of the simulation.

The results have not been reported in tables, since the panels assume an unreal behavior, intersecting and overlapping very quickly and consequently the simulated behavior is not plausible. Figure 3.1 report two instantaneous of the 3D animation output, in order to show the behavior of the panel.

## 3.2 SIMULATIONS WITH PANELS OF DIFFERENT THICKNESSES

Before analyzing the performances of an actively controlled solar array, which adds complexity to the overall system, the possibility to control the panels with their simple stiffening was examined. Some thicknesses were chosen in order to establish which was the optimal configuration: 100  $\mu\text{m}$ , 200  $\mu\text{m}$  and 500  $\mu\text{m}$ . Being the panel stiffened, its mass increases as reported in table 2.4. It is not a great issue in the case of large satellites, but it became an important point if the total spacecraft mass has to be low.

The results of the simulations reported below are divided by height as in the previous case, since the study was made comparing the behavior of the satellite subjected to the same conditions, in particular in terms of dimension of the panels and disturbances.

The parameters considered in the tables are defined as follows:

- $\delta x_L$  and  $\delta x_R$  are the deflections performed respectively by the left and right panel tip;
- $T_{pL}$  and  $T_{pR}$  represent the Y component of the torque transmitted respectively from the left and right panel to the satellite (the other two components result negligible);
- $T_c$  is the Y component of the torque necessary for the attitude control system of the central body to maintain the nominal pointing and is related to the authority needed for the actuator. This torque represents the vector sum of the torques transmitted from both the panels to the central body, if the latter was not affected by any disturbances.

The most meaningful results are reported in the following tables. If not indicated otherwise, they refer to the first peak of

$s$ [ $\mu\text{m}$ ]	$\delta x_L$ [m]	$\delta x_R$ [m]	$T_{pL}$ [N m]	$T_{pR}$ [N m]	$T_c$ [N m]
100	-	-	-	-	-
200	-	-	-	-	-
500	0.60	0.60	4.47 E-3	4.47 E-3	6.74 E-4

**Table 3.1:** Results of the simulations at 300 km altitude with inertial attitude.

$s$ [ $\mu\text{m}$ ]	$\delta x_L$ [m]	$\delta x_R$ [m]	$T_{pL}$ [N m]	$T_{pR}$ [N m]	$T_c$ [N m]
100	-	-	-	-	-
200	3.40	-	1.76 E-3	-	-
500	0.54	0.68	3.82 E-3	4.96 E-3	4.93 E-3

**Table 3.2:** Results of the simulations at 300 km altitude with nadir-pointing attitude with the satellite inclined by  $45^\circ$ . In this table the maximum values collected during the first 1000 seconds are reported.

oscillation, which is generally the maximum value or reasonably close to it. Each table is then supported by the associated figures reported at the end of the chapter, that report the time behavior of the results collected during one orbit period.

### 3.2.1 Simulations in low LEO

In this section the results related to the simulations with the satellite subjected to the drag force are presented. In particular, in table 3.1 the results refer to the inertial attitude condition, while in table 3.2 they refer to a nadir-pointing satellite.

The results of the simulations which consider the 100  $\mu\text{m}$  and 200  $\mu\text{m}$  thick panels are not reported in table 3.1, because the panels oscillate excessively and overlap at 300 km altitude. The blue and green lines in figures 3.2 and 3.3 confirm this irregular behavior, which is also reflected in figures 3.4, 3.5 and 3.6. The panel on the right is the first which become unstable since the force applied on it tends to take it in the opposite direction with respect to the straight position (see figure 3.3). The torques transmitted from the panels to the satellite are relatively high for a small spacecraft, on the order of  $10^{-3}$  N m. The control torques  $T_c$  necessary for the control system of the satellite to keep the nominal pointing, i.e. the vector sum of  $T_{pL}$  and  $T_{pR}$ , result on the order of  $10^{-4}$  N m.

$s$ [ $\mu\text{m}$ ]	$\delta x_L$ [m]	$\delta x_R$ [m]	$T_{pL}$ [Nm]	$T_{pR}$ [Nm]	$T_c$ [Nm]
100	1.38	1.49	6.87 E-5	7.13 E-5	8.76 E-6
200	0.18	0.19	7.36 E-5	7.70 E-5	1.84 E-5
500	0.01	0.01	7.99 E-5	8.77 E-5	4.45 E-5

**Table 3.3:** Results of the simulations at 750 km altitude with inertial attitude.

From figure 3.7 to 3.11 and from table 3.2 it is possible to deduct that 100  $\mu\text{m}$  thick panels on a nadir-pointing satellite are not stiff enough to stand the drag force at 300 km altitude. In the second case, with 200  $\mu\text{m}$  thick panels, the left one performs wide oscillations without losing control, while the right one becomes immediately unusable. The orientation imposed to the satellite causes torques of higher intensity on the right panel, because the surface area of this panel exposed to the atmospheric drag increases while oscillating, on the contrary on the other panel the surface decreases. This behavior is confirmed in figure 3.9 and 3.10. This is the case in which the control torques on the panels are higher, reaching  $10^{-3}$  Nm.

### 3.2.2 Simulations in high LEO

Increasing the height, simulations are performed considering the other three fundamental disturbances.

Since the solar radiation pressure depends on the exposure of the panel to the sunlight, being the orbits circular and equatorial, the proper light and shade time is considered. The transition is clearly visible in the figures that follow, since the component of the force due to the solar radiation pressure does not give its contribution while the satellite is not illuminated.

The damping coefficients of the material about X and Z body axes are sufficiently high to effectively damp the small torques exerted along X and Z directions, which are especially due to the coupling between the residual magnetic dipole of the panels and the Earth's magnetic field.

The different behavior in terms of torques transmitted from the panels to the satellite is due to the different coupling between the torques caused in particular by the gravity gradient and the solar radiation pressure in the two panels. At time  $t = 0$  the forces due to the gravity gradient and the solar radiation pressure are perfectly summed. During the light periods,

$s$ [ $\mu\text{m}$ ]	$\delta x_L$ [m]	$\delta x_R$ [m]	$T_{pL}$ [N m]	$T_{pR}$ [N m]	$T_c$ [N m]
100	1.54	1.22	$7.20 \text{ E}-5$	$5.78 \text{ E}-5$	$1.65 \text{ E}-5$
200	0.23	1.14	$8.43 \text{ E}-5$	$5.25 \text{ E}-5$	$3.42 \text{ E}-5$
500	0.02	$4.6 \text{ E}-3$	$1.09 \text{ E}-4$	$2.91 \text{ E}-5$	$8.55 \text{ E}-5$

**Table 3.4:** Results of the simulations at 750 km altitude with nadir pointing attitude.

the gravity gradient force vector  $\vec{F}_{g, \text{panel}}$  rotates with respect to the solar radiation force vector  $\vec{F}_{\text{rp}}$ . In the night period the solar radiation pressure is null. The torques due to the residual magnetic field on the panels are summed to the other two disturbances, but their contribution is very limited.

#### *Other results*

Other simulations were performed at different heights, but the trend was almost the same with respect to the results of the simulations at 750 km altitude, and for this reason the figures are not reported. In tables 3.5 and 3.6 the results of the simulations at 1000 km height are reported.

$s$ [ $\mu\text{m}$ ]	$\delta x_L$ [m]	$\delta x_R$ [m]	$T_{pL}$ [N m]	$T_{pR}$ [N m]	$T_c$ [N m]
100	1.59	1.70	$6.84 \text{ E}-5$	$7.40 \text{ E}-5$	$8.05 \text{ E}-6$
200	0.20	0.23	$6.92 \text{ E}-5$	$8.03 \text{ E}-5$	$1.80 \text{ E}-5$
500	0.01	0.02	$6.96 \text{ E}-5$	$9.06 \text{ E}-5$	$4.29 \text{ E}-5$

**Table 3.5:** Results of the simulations at 1000 km altitude with inertial attitude.

$s$ [ $\mu\text{m}$ ]	$\delta x_L$ [m]	$\delta x_R$ [m]	$T_{pL}$ [N m]	$T_{pR}$ [N m]	$T_c$ [N m]
100	1.75	1.42	$7.42 \text{ E}-5$	$6.08 \text{ E}-5$	$1.66 \text{ E}-5$
200	0.26	0.16	$8.72 \text{ E}-5$	$5.64 \text{ E}-5$	$3.31 \text{ E}-5$
500	0.02	$5.99 \text{ E}-3$	$1.11 \text{ E}-4$	$3.39 \text{ E}-5$	$8.26 \text{ E}-5$

**Table 3.6:** Results of the simulations at 1000 km altitude with nadir pointing attitude.

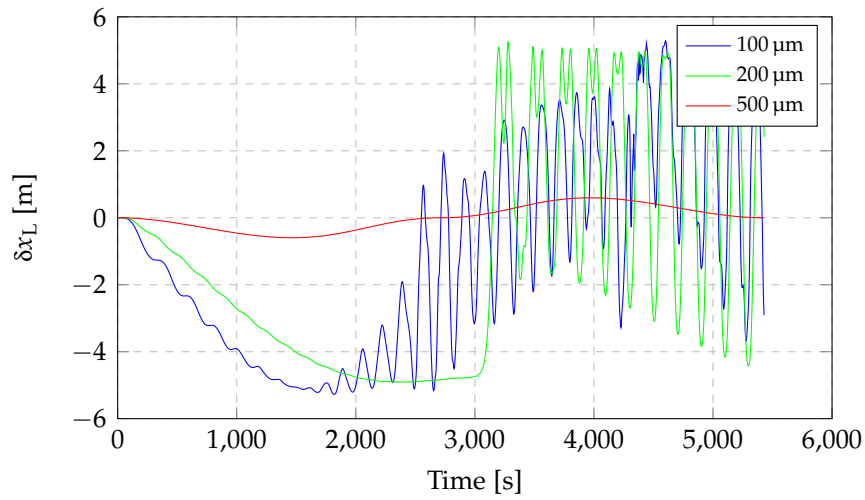


Figure 3.2: Displacements of the left tip at 300 km altitude with inertial attitude (see table 3.1).

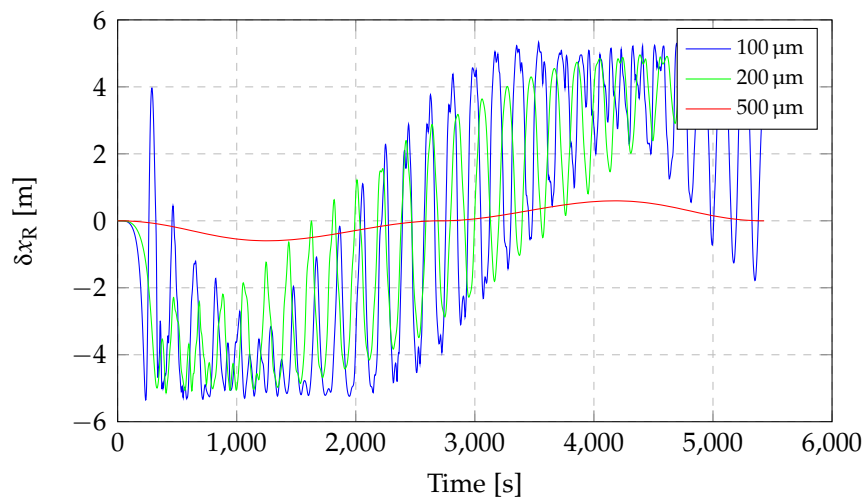


Figure 3.3: Displacements of the right tip at 300 km altitude with inertial attitude (see table 3.1).

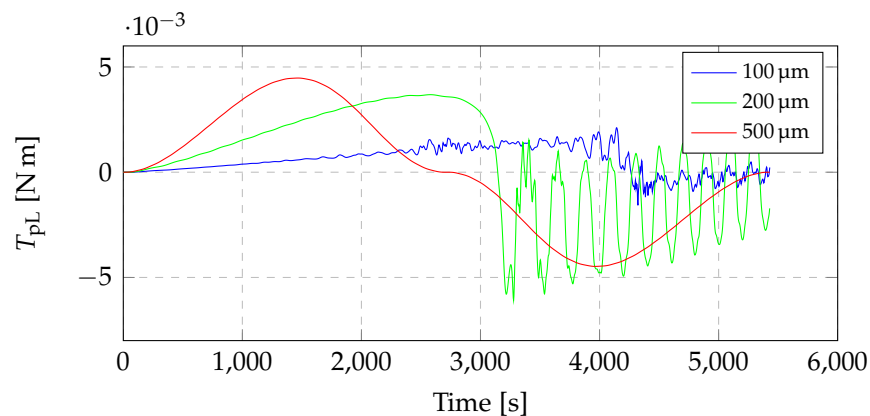


Figure 3.4: Torques transferred from the left panel to the central body at 300 km altitude with inertial attitude (see table 3.1).

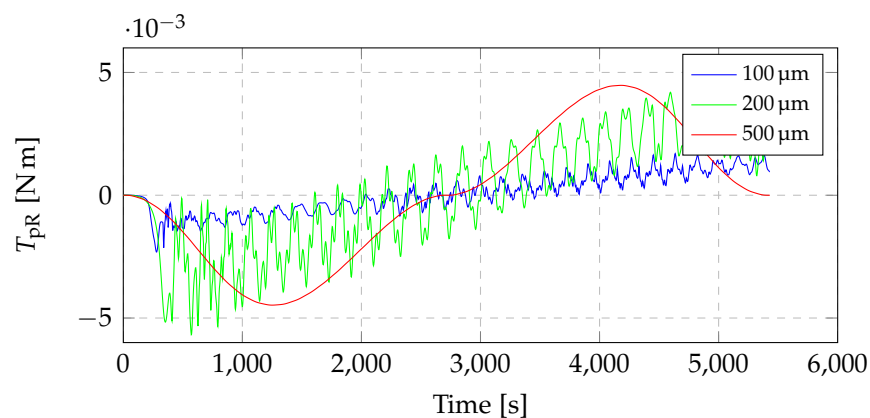


Figure 3.5: Torques transferred from the right panel to the central body at 300 km altitude with inertial attitude (see table 3.1).

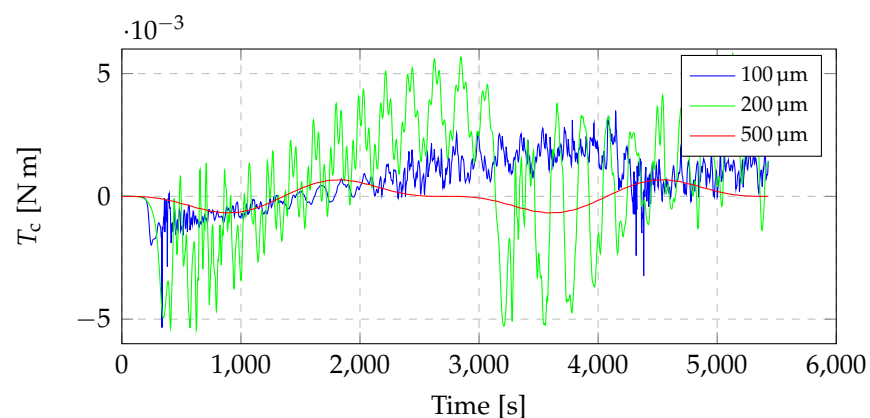


Figure 3.6: Control torques on the satellite at 300 km altitude with inertial attitude (see table 3.1).

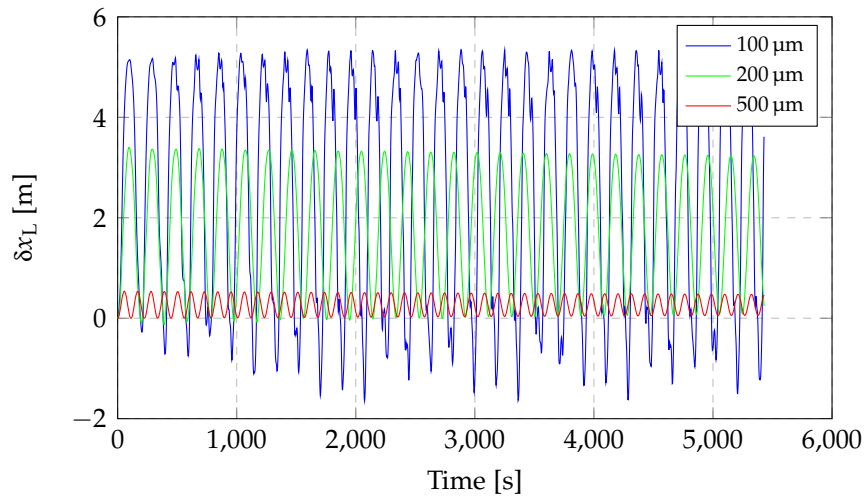


Figure 3.7: Displacements of the left tip at 300 km altitude (see table 3.2).

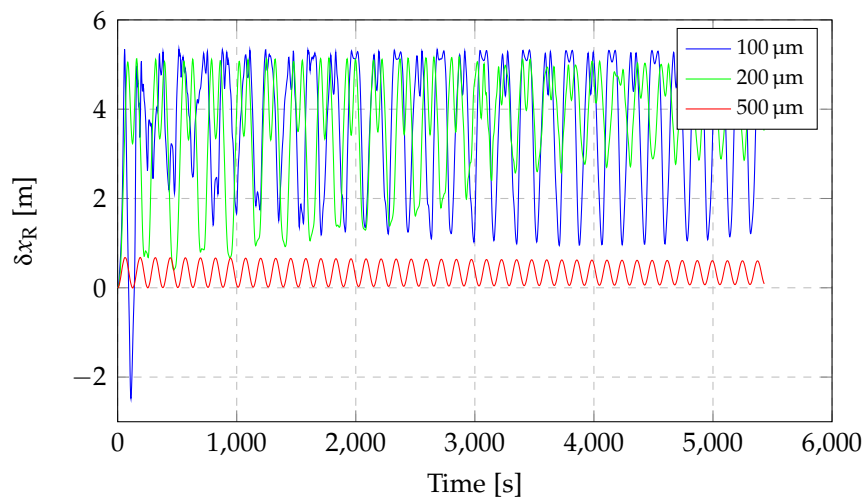


Figure 3.8: Displacements of the right tip at 300 km altitude (see table 3.2).

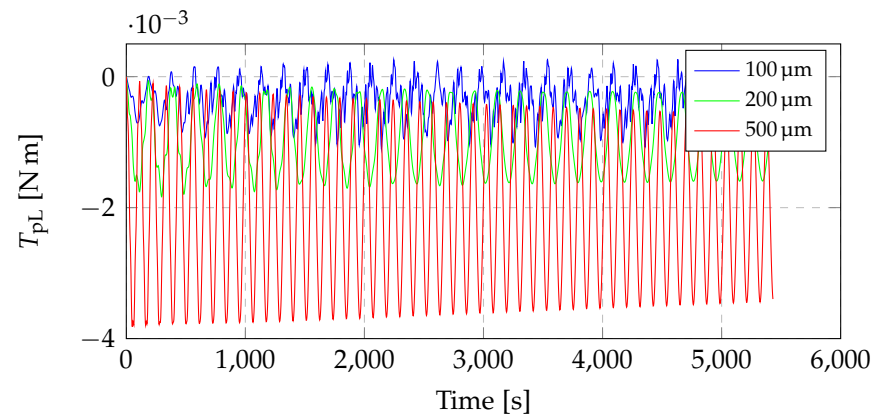


Figure 3.9: Torques transferred from the left panel to the central body at 300 km altitude with nadir pointing attitude (see table 3.2).

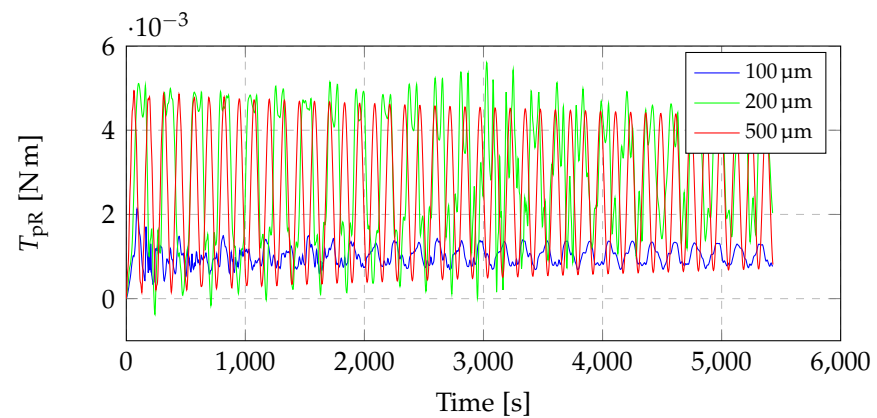


Figure 3.10: Torques transferred from the right panel to the central body at 300 km altitude with nadir pointing attitude (see table 3.2).

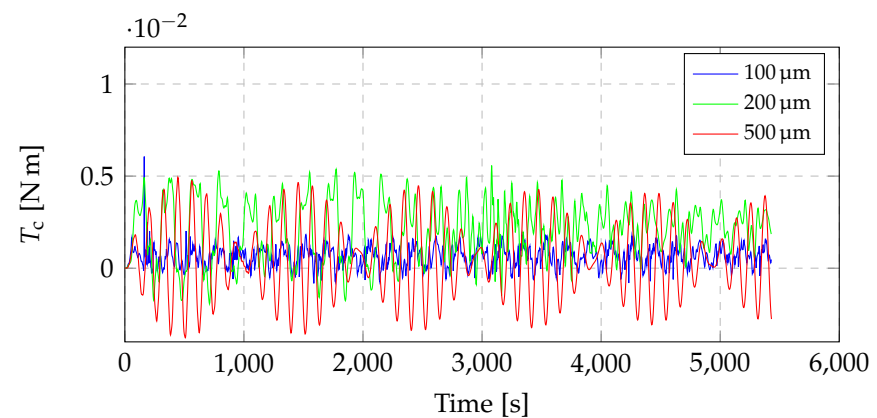


Figure 3.11: Control torques on the satellite (see table 3.2).

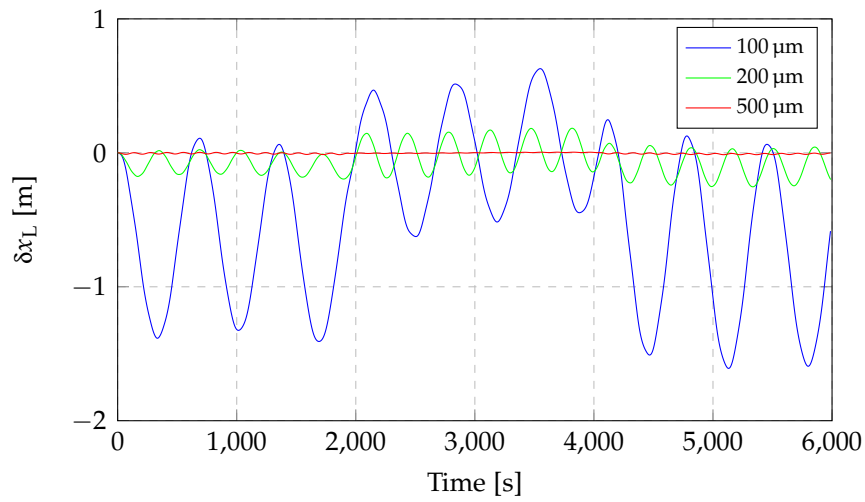


Figure 3.12: Displacements of the left tip at 750 km altitude (see table 3.3).

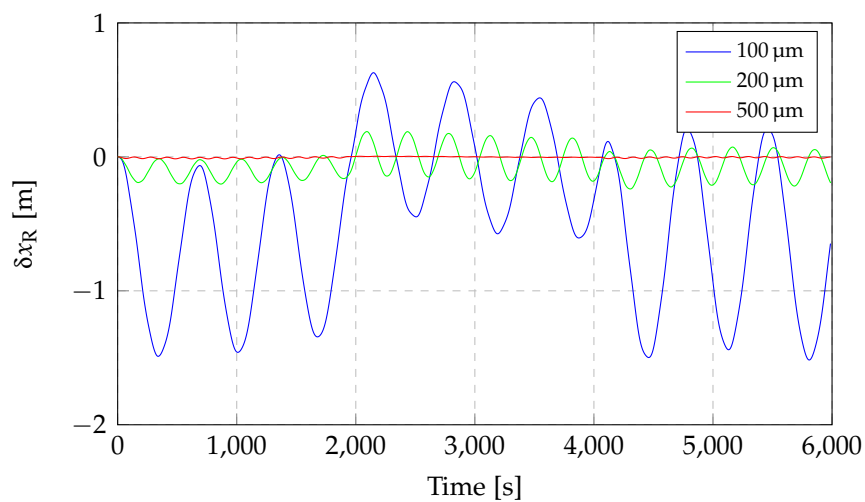


Figure 3.13: Displacements of the right tip at 750 km altitude (see table 3.3).

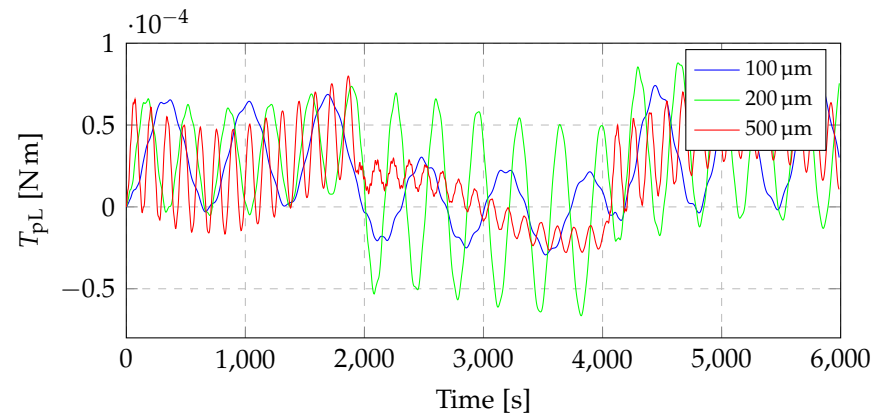


Figure 3.14: Torques transferred from the left panel to the central body (see table 3.3).

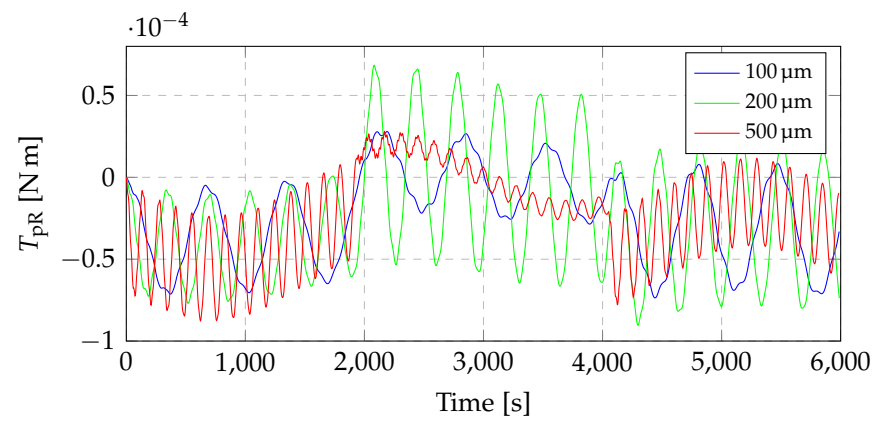


Figure 3.15: Torques transferred from the right panel to the central body (see table 3.3).

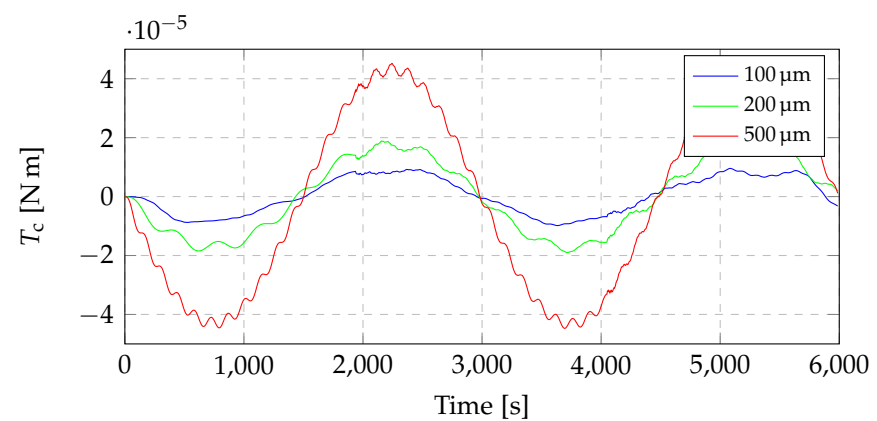


Figure 3.16: Control torques on the satellite (see table 3.3).

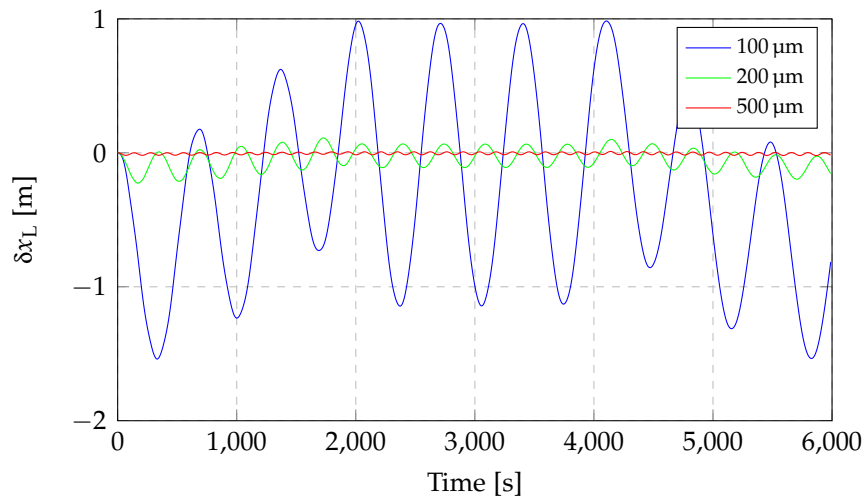


Figure 3.17: Displacements of the left tip at 750 km altitude (see table 3.4).

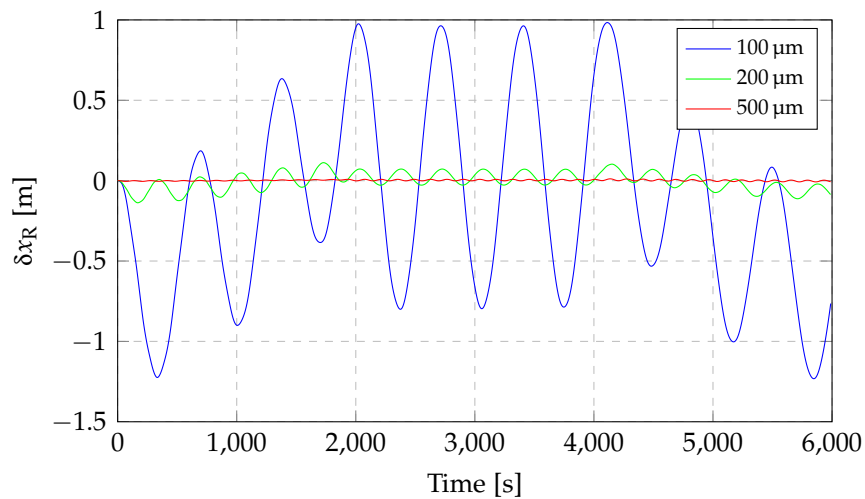


Figure 3.18: Displacements of the right tip at 750 km altitude (see table 3.4).

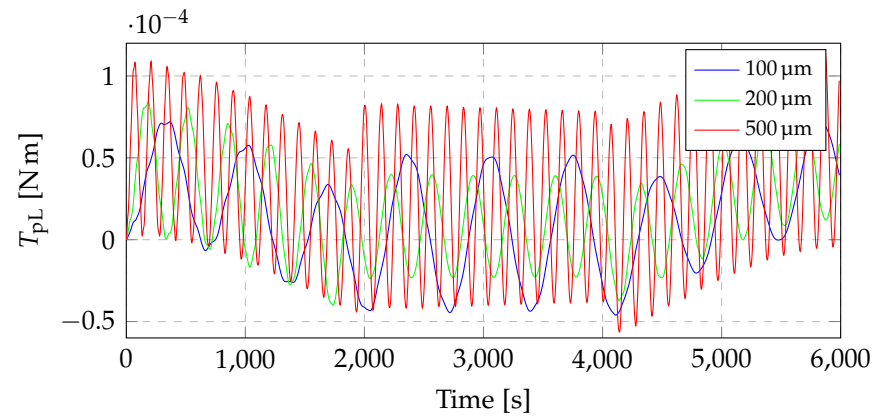


Figure 3.19: Torques transferred from the left panel to the central body (see table 3.4).

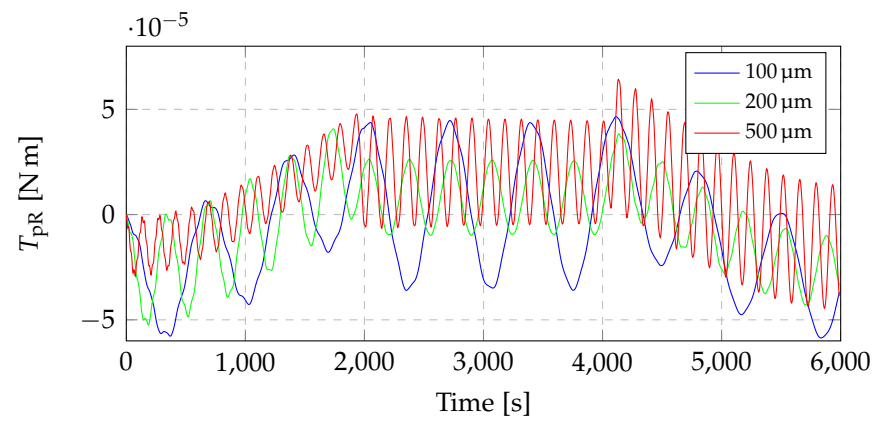


Figure 3.20: Torques transferred from the right panel to the central body (see table 3.4).

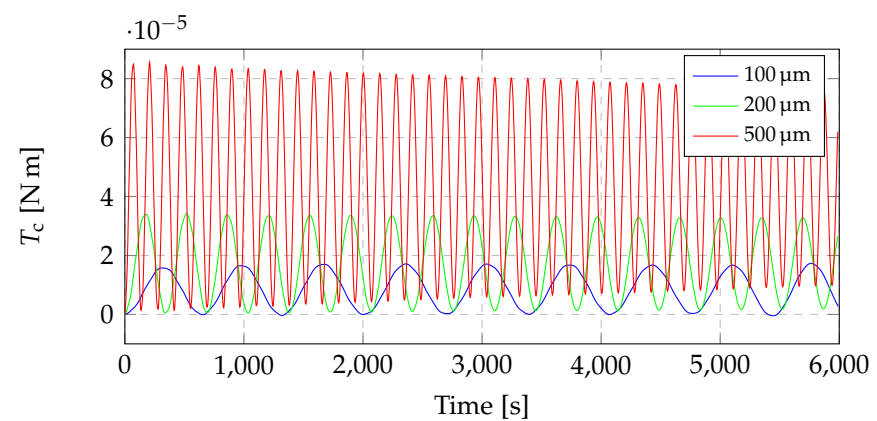


Figure 3.21: Control torques on the satellite (see table 3.4).

# 4

## SIMULATIONS WITH ACTIVE VIBRATIONS CONTROL SYSTEM

The aim of the simulations presented in this chapter is to better understand if it is convenient to provide the panel with an active control system and if it is a valid alternative to the simple thickening of the panel.

The simulations in this chapter are executed neglecting the contribution in terms of mass, volume and stiffness due to the material of the control system, thought as a distributed linear control. It should be stressed that it could change the characteristics of the panel, depending on which control configuration is adopted.

The control system is implemented on each joint as a proportional - derivative (PD) control law. The control is performed only on the bending around *Y Body* axis, since the disturbances on the *Z Body* axis are principally due to the magnetic field contribution in the present simulations create a negligible torsion.

The gains applied on the controller are chosen in order to minimize the oscillations, and in general are:  $K_p = 10^{-1} \div 10^{-3}$  (proportional gain) and  $K_d = 10^{-4}$  (derivative gain). Therefore, the control system receives as input the instantaneous difference in the *X Body* direction between the coordinates of the two extreme points of the single body. It is equivalent of giving in input to the control system the rotation angle of each joint. The control system can be thought as another parallel of spring and damper, where  $K_p$  and  $K_d$  are the stiffness and damping coefficients respectively.

In SimMechanics™ environment the PD controller is a block that produces as output the signal:

$$T_{pc} = \delta x \cdot \left( K_p + K_d \cdot \frac{N}{1 + N \frac{1}{s}} \right) \quad (4.1)$$

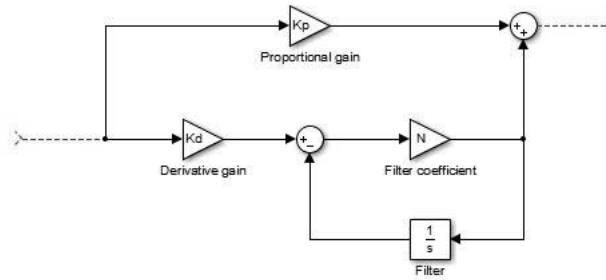


Figure 4.1: PD controller block system.

where  $N$  is a filter coefficient. The controller is represented by the blocks system in figure 4.1 and is connected to the joint actuator as shown in figure 2.1.

Increasing the gains of the PD controllers, in particular  $K_p$ , in general the actuators improve their performances, damping the oscillations more efficiently and stabilizing the 25  $\mu\text{m}$  thick panels at low altitude, which could not be used without a control system or shows wide oscillations. On the other hand, increasing  $K_d$  the time needed for the damping of oscillations reduces. Nevertheless, gains cannot be incremented arbitrarily, because such a control system becomes useless. For this reason, the simulations have been performed varying  $K_p$  both with the altitude and the attitude. In particular, the choice of the gains have been done analyzing both the deformations and the torques induced on the central body.

In the following sections, the parameters  $T_{pcL}$  and  $T_{pcR}$  represent the torque exerted by the control system on the connecting joint between the central body and the left and right panel respectively. They represent the maximum torque needed to control the panels.

The figures are reported at the end of the chapter.

#### 4.1 RESULTS OF THE SIMULATIONS WITH AN ACTIVELY CONTROLLED SYSTEM

The simulations are performed varying the authority of the control system. In the figure legends, PD<sub>1</sub>, PD<sub>2</sub> and PD<sub>3</sub> refer to the authority of the simulated control systems, listed in the same order of the results in the related tables.

## 4.1.1 Simulations in low LEO

The simulations at 300 km altitude have been executed with a satellite subjected only to the drag force, as in the previous chapter.

In this section, PD<sub>1</sub>, PD<sub>2</sub> and PD<sub>3</sub> are defined as in table 4.1.

	$K_p$	$K_d$
PD <sub>1</sub>	2.5 E-2	1 E-4
PD <sub>2</sub>	5.0 E-2	1 E-4
PD <sub>3</sub>	7.5 E-2	1 E-4

Table 4.1: Authority of the control system of the panels in low LEO.

The coefficients of PD<sub>1</sub> control system (blue lines in the figures from 4.2 to 4.8) were chosen in order to obtain the same displacements of the configuration in which panels with 500  $\mu\text{m}$  of thickness were simulated. On the other hand, the authority of PD<sub>2</sub> and PD<sub>3</sub> is slightly higher, and this means that the displacements reduce (green and red lines in the figures 4.2 and 4.3), with a consequent decrease of the torques necessary for the satellite to maintain the desired pointing (figure 4.7). The curves that represent the torques transferred from the panels to the satellite in figure 4.4 and 4.5 result almost overlapped in the three cases, because the drag force depends essentially on the surface exposed to it, which is very similar in the case of limited displacements. Their difference represents the torque necessary for the control system of the satellite to keep the nominal pointing, as shown in figure 4.6. Consequently, the torque exerted by the PD control system of the panels is approximately equal in modulus and opposite in sign with respect to the transmitted torque. This behavior is reported in figures 4.7 and 4.8.

In figures from 4.9 to 4.15 the results of the simulations with nadir-pointing attitude are reported. Blue lines in figures represent a system with similar displacements with respect to the stiffened configuration with a cross section of 500  $\mu\text{m}$ . Again, two other configurations (PD<sub>2</sub> and PD<sub>3</sub>) with higher stiffness and damping coefficients are presented with green and red lines. In all the three cases the control torques exerted by the control system of the panels result similar, since the torque transferred from the panel to the central body do not vary significantly, as the displacements are limited.

$\delta x_L$ [m]	$\delta x_R$ [m]	$T_{pL}$ [N m]	$T_{pR}$ [N m]	$T_c$ [N m]	$T_{pCL}$ [N m]	$T_{pCR}$ [N m]
0.57	0.57	4.44E-3	4.44E-3	6.31E-4	4.43E-3	4.43E-3
0.28	0.28	4.47E-3	4.47E-3	3.20E-4	4.46E-3	4.46E-3
0.19	0.19	4.47E-3	4.47E-3	2.14E-4	4.47E-3	4.47E-3

Table 4.2: Results of the simulations at 300 km altitude with inertial attitude.

$\delta x_L$ [m]	$\delta x_R$ [m]	$T_{pL}$ [N m]	$T_{pR}$ [N m]	$T_c$ [N m]	$T_{pCL}$ [N m]	$T_{pCR}$ [N m]
0.53	0.61	3.98E-3	4.90E-3	5.09E-3	3.97E-3	4.90E-3
0.27	0.30	4.19E-3	4.65E-3	4.83E-3	4.19E-3	4.65E-3
0.19	0.19	4.28E-3	4.57E-3	4.71E-3	4.28E-3	4.57E-3

Table 4.3: Results of the simulations at 300 km altitude with nadir pointing attitude.

#### 4.1.2 Simulations in high LEO

The simulations at 750 km altitude have been executed with a satellite subjected to solar radiation pressure, gravity gradient force and the torque due to the residual magnetic dipole on the panels, as in the previous chapters.

In this section, the authority of the control systems PD<sub>1</sub>, PD<sub>2</sub> and PD<sub>3</sub> are reported in table 4.4.

	$K_p$	$K_d$
PD <sub>1</sub>	1 E-3	1 E-4
PD <sub>2</sub>	5 E-3	1 E-4
PD <sub>3</sub>	1 E-2	1 E-4

Table 4.4: Authority of the control system of the panels in high LEO.

In these simulations, the coefficients  $K_p$  and  $K_d$  of the first case PD<sub>1</sub> were chosen in order to show a similar behavior in terms of displacements of the stiffened system with 200  $\mu\text{m}$  thick panels. On the other hand, the third case PD<sub>3</sub> shows similar tip displacements of the stiffened system with a panel cross section of 500  $\mu\text{m}$ . As a consequence to the higher  $K_p$  parameters, displacements reduce as shown in figures 4.16-4.17 and 4.23-4.24.

$\delta x_L$ [m]	$\delta x_R$ [m]	$T_{pL}$ [N m]	$T_{pR}$ [N m]	$T_c$ [N m]	$T_{pcl}$ [N m]	$T_{pcr}$ [N m]
0.23	0.23	6.96E-5	6.98E-5	4.61E-6	6.85E-5	6.88E-5
0.04	0.04	6.98E-5	6.98E-5	3.44E-6	6.96E-5	6.97E-5
0.02	0.02	6.98E-5	6.98E-5	3.26E-6	6.97E-5	6.98E-5

Table 4.5: Results of the simulations at 750 km altitude with inertial attitude.

$\delta x_L$ [m]	$\delta x_R$ [m]	$T_{pL}$ [N m]	$T_{pR}$ [N m]	$T_c$ [N m]	$T_{pcl}$ [N m]	$T_{pcr}$ [N m]
0.23	0.22	7.16E-5	6.74E-5	4.42E-6	7.04E-5	6.64E-5
0.05	0.04	7.19E-5	6.77E-5	4.68E-6	7.17E-5	6.75E-5
0.02	0.02	7.20E-5	6.78E-5	4.69E-6	7.19E-5	6.77E-5

Table 4.6: Results of the simulations at 750 km altitude with nadir pointing attitude.

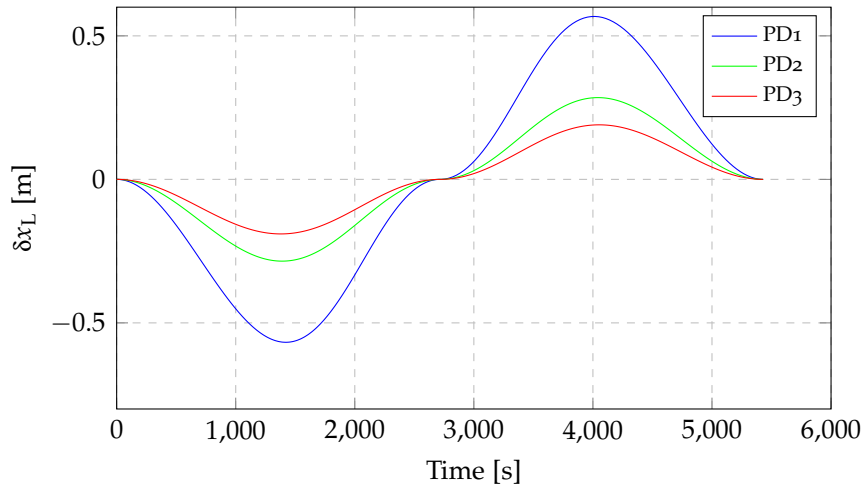


Figure 4.2: Displacements of the left tip at 300 km altitude with inertial attitude with controlled systems (see table 4.2).

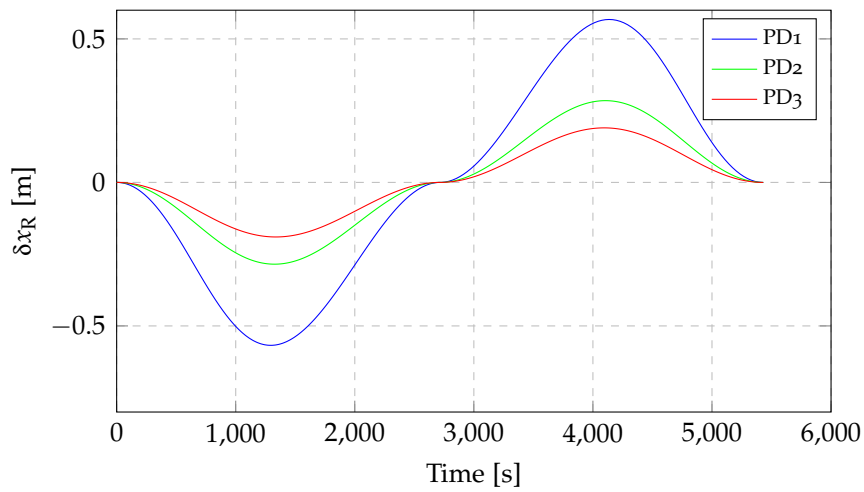


Figure 4.3: Displacements of the right tip at 300 km altitude with inertial attitude with controlled systems (see table 4.2).

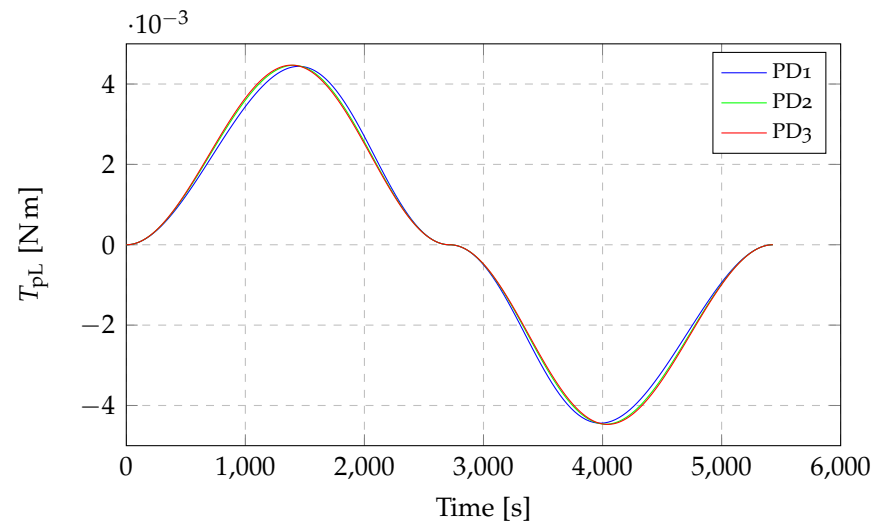


Figure 4.4: Torques transferred from the left panel to the central body at 300 km altitude with inertial attitude (see table 4.2).

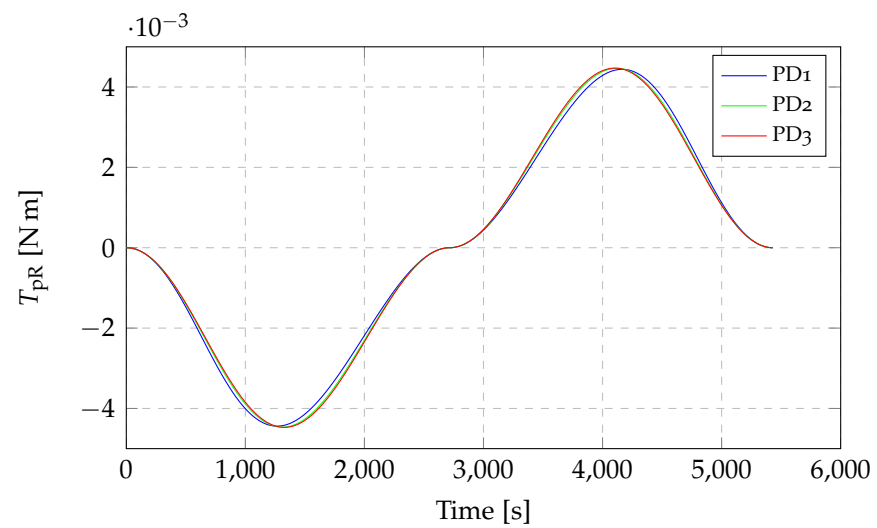


Figure 4.5: Torques transferred from the right panel to the central body at 300 km altitude with inertial attitude (see table 4.2).

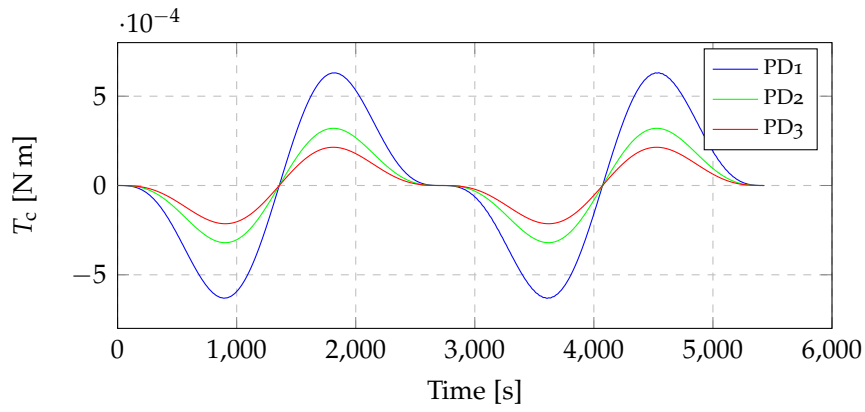


Figure 4.6: Control torques on the satellite at 300 km altitude with inertial attitude (see table 4.2).

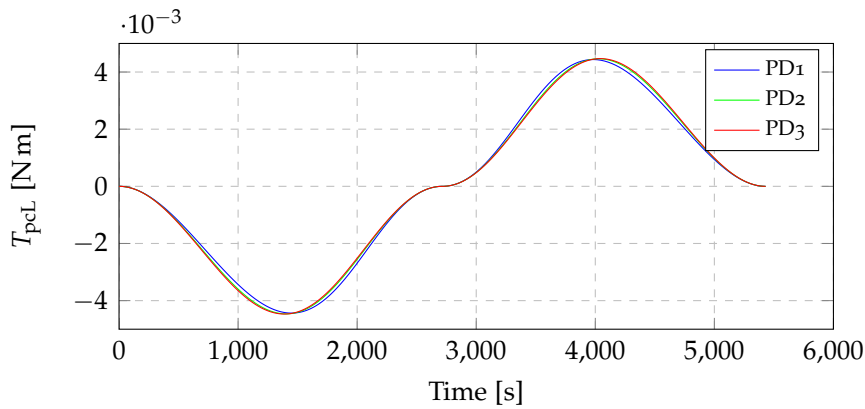


Figure 4.7: Control torques exerted by the control system on the connecting joint between the left panel and the central body (see table 4.2).

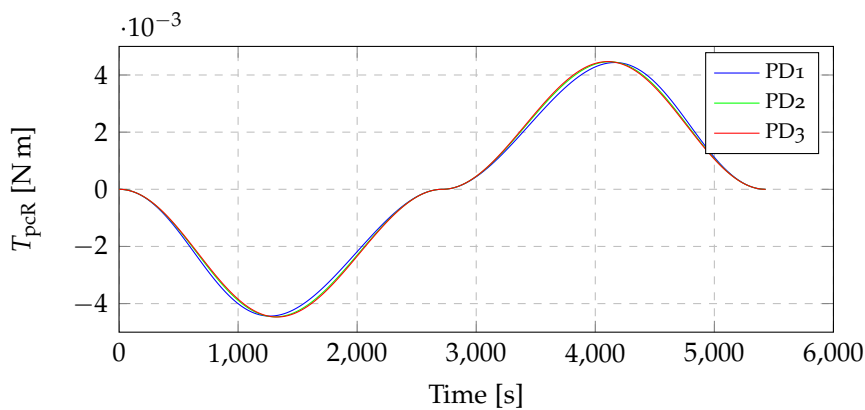


Figure 4.8: Control torques exerted by the control system on the connecting joint between the right panel and the central body (see table 4.2).

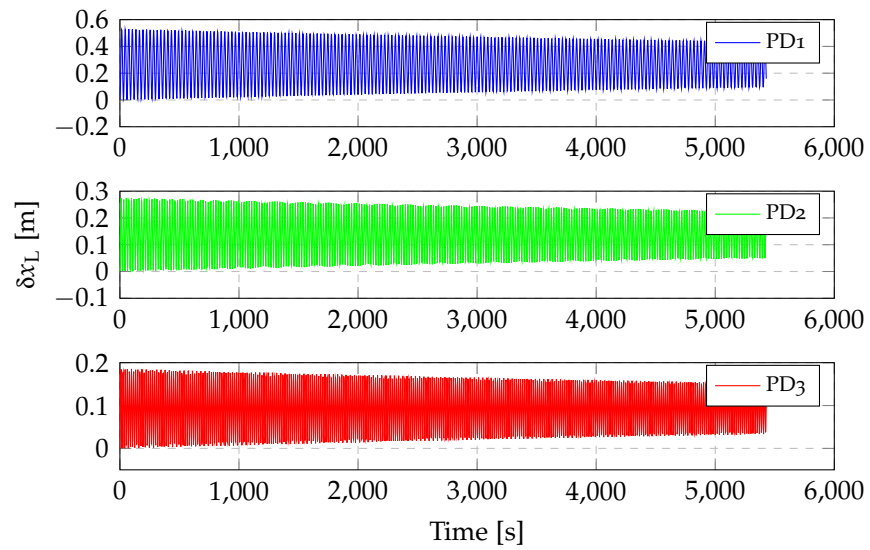


Figure 4.9: Displacements of the left tip at 300 km altitude with nadir pointing attitude with controlled systems (see table 4.3).

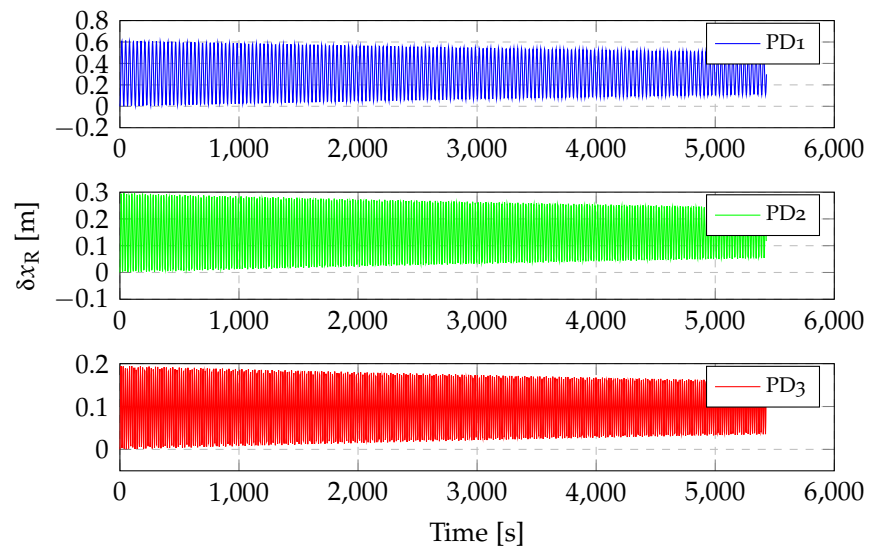


Figure 4.10: Displacements of the right tip at 300 km altitude with nadir pointing attitude with controlled systems (see table 4.3).

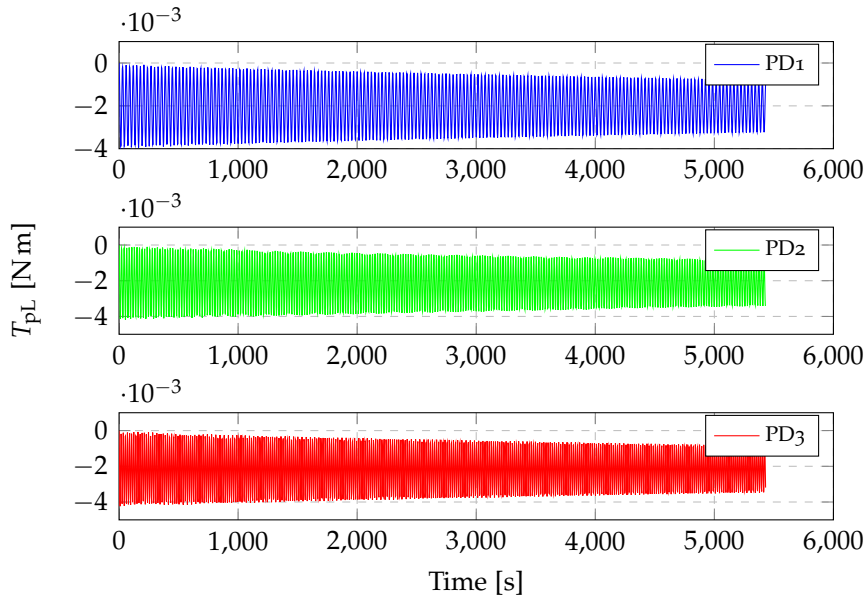


Figure 4.11: Torques transferred from the left panel to the central body at 300 km altitude with nadir pointing attitude (see table 4.3).

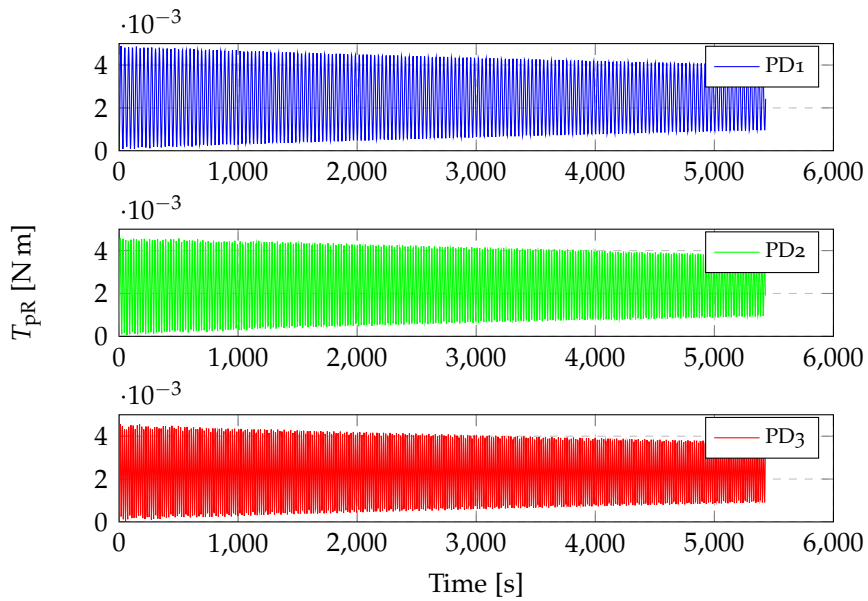


Figure 4.12: Torques transferred from the right panel to the central body at 300 km altitude with nadir pointing attitude (see table 4.3).

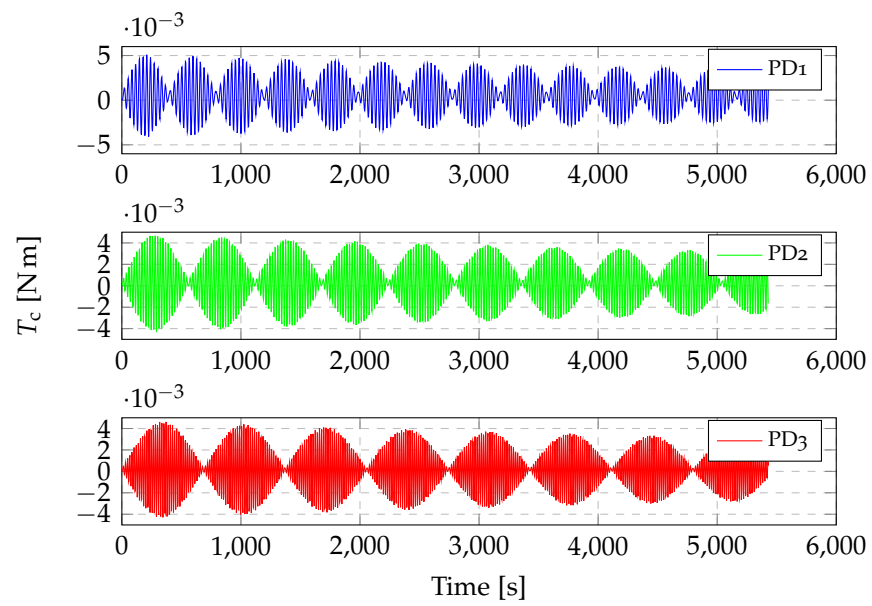


Figure 4.13: Control torques on the satellite at 300 km altitude with nadir pointing attitude (see table 4.3).

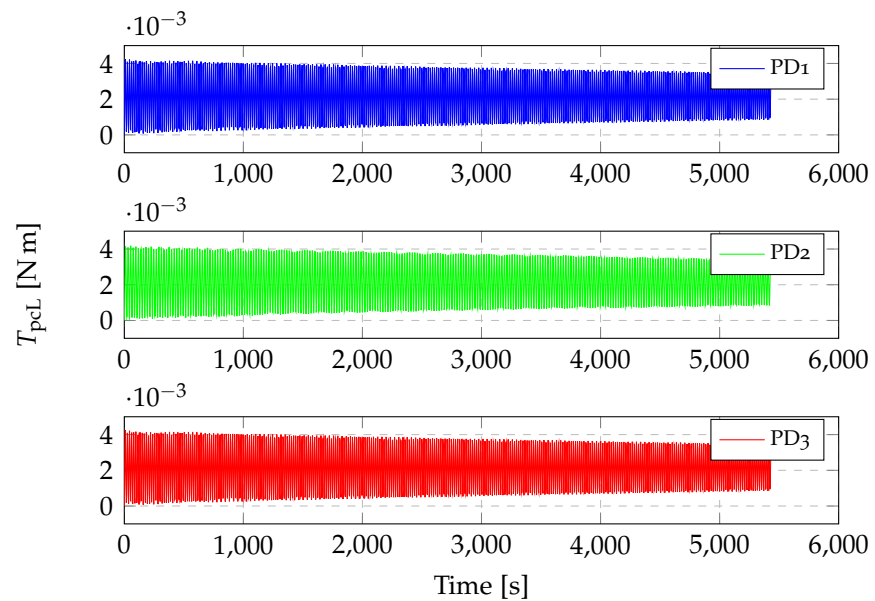


Figure 4.14: Control torques exerted by the control system on the connecting joint between the left panel and the central body (see table 4.3).

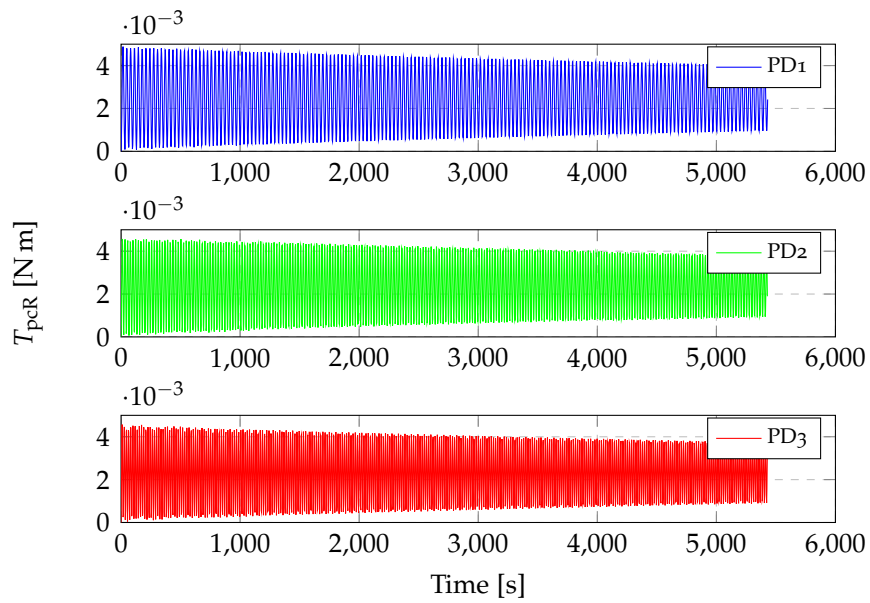


Figure 4.15: Control torques exerted by the control system on the connecting joint between the right panel and the central body (see table 4.3).

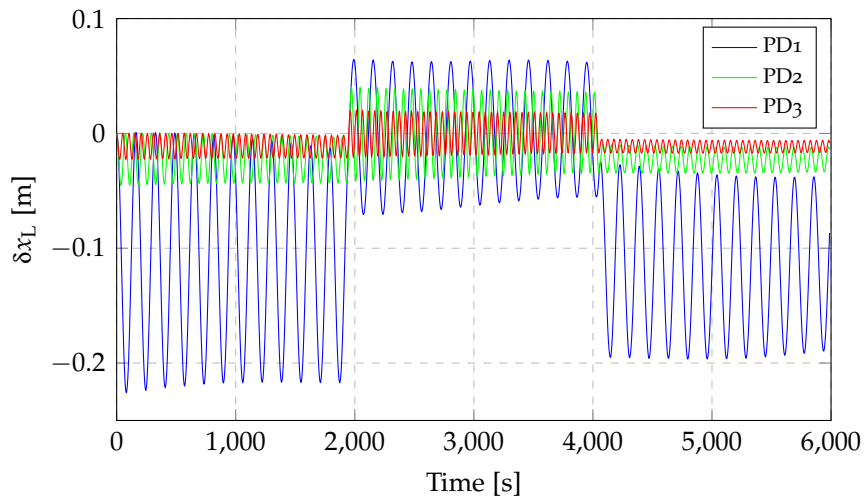


Figure 4.16: Displacements of the left tip at 750 km altitude with inertial attitude with controlled systems (see table 4.5).

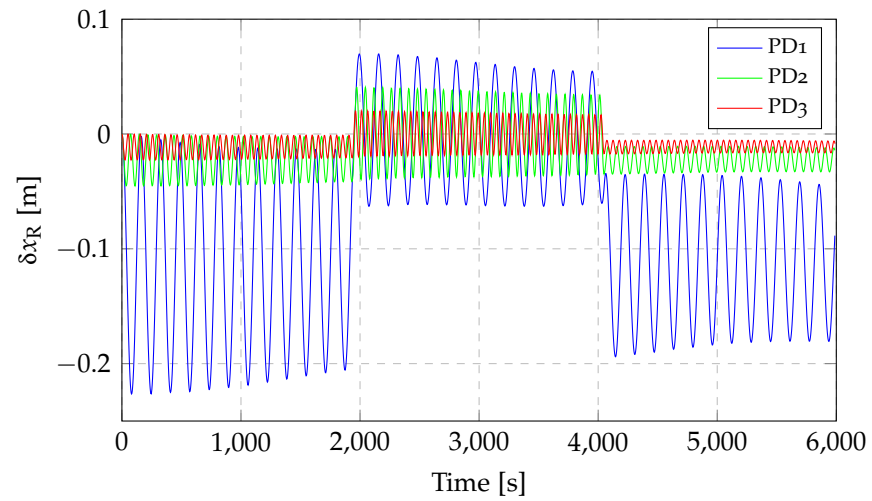


Figure 4.17: Displacements of the right tip at 750 km altitude with inertial attitude with controlled systems (see table 4.5).

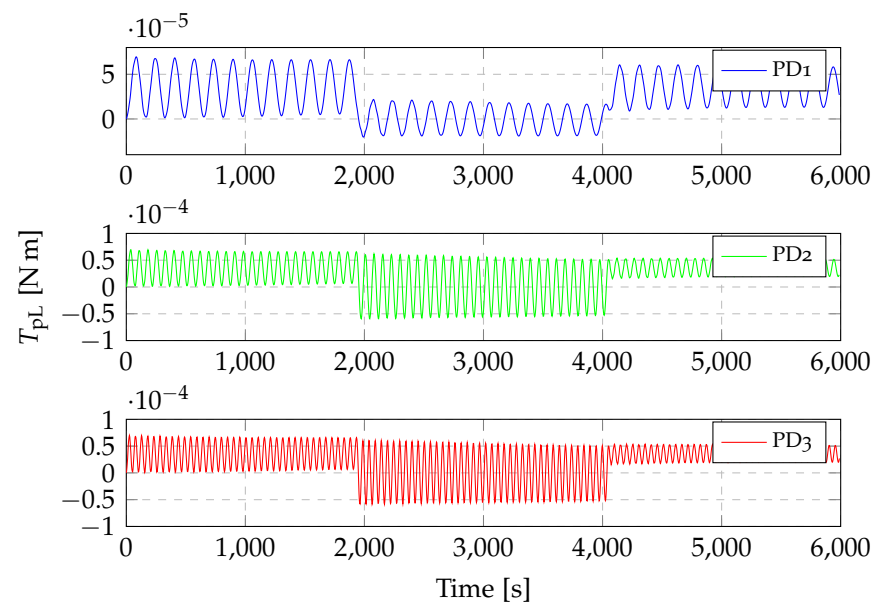


Figure 4.18: Torques transferred from the left panel to the central body at 750 km altitude with inertial attitude (see table 4.5).

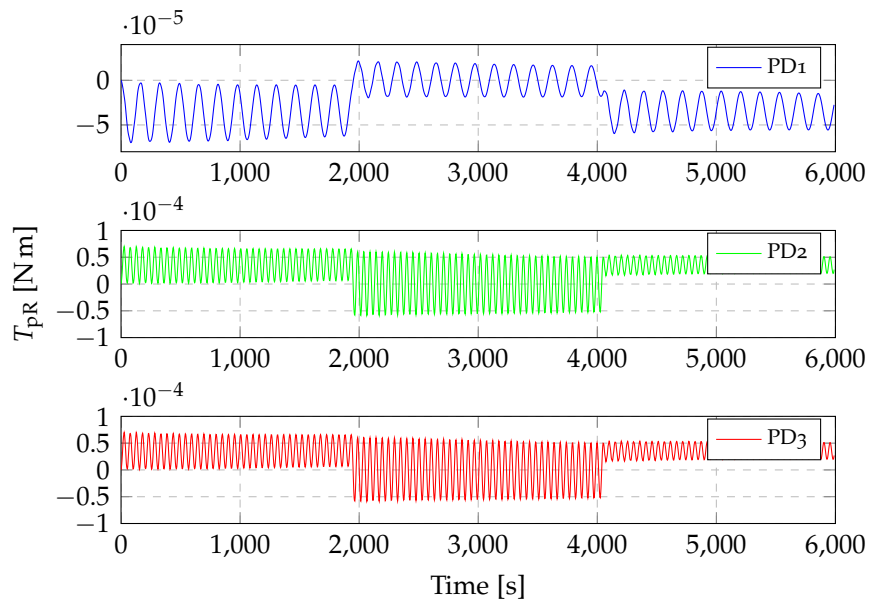


Figure 4.19: Torques transferred from the right panel to the central body at 750 km altitude with inertial attitude (see table 4.5).

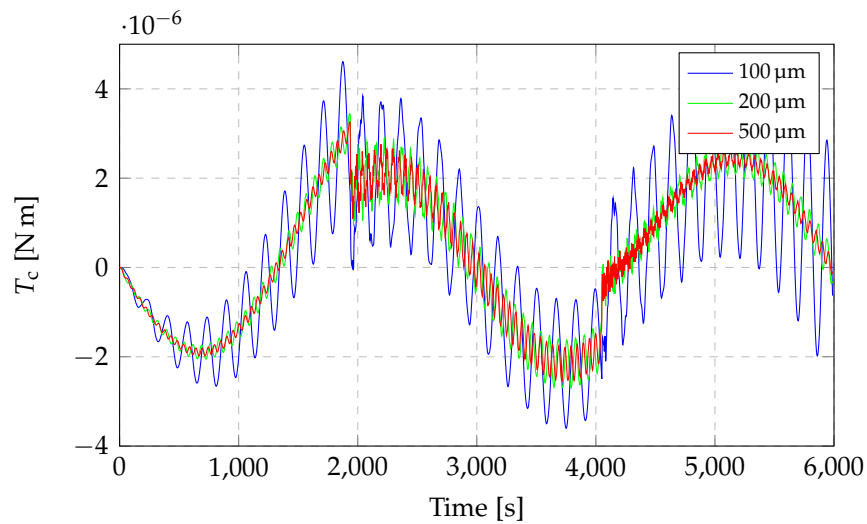


Figure 4.20: Control torques on the satellite at 750 km altitude with inertial attitude (see table 4.5).

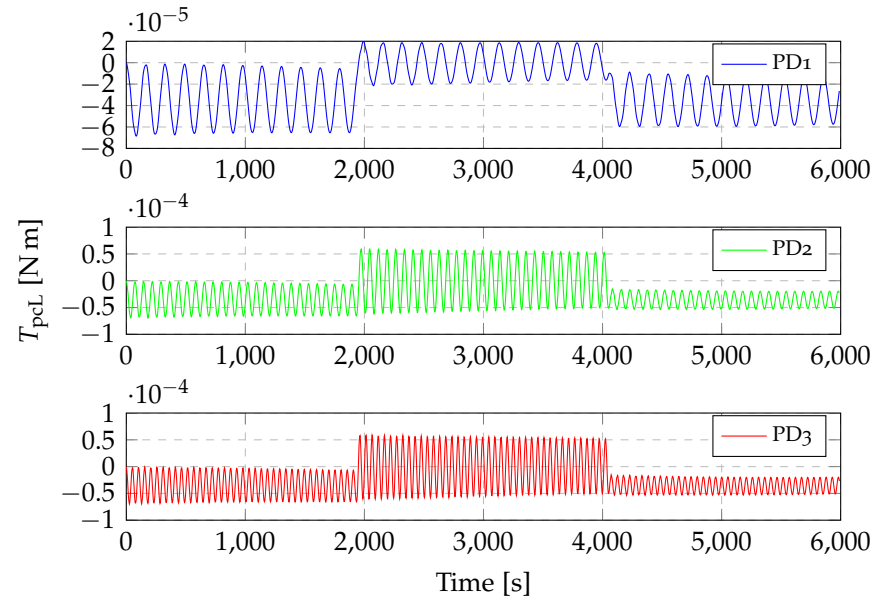


Figure 4.21: Control torques exerted by the control system on the connecting joint between the left panel and the central body (see table 4.5).

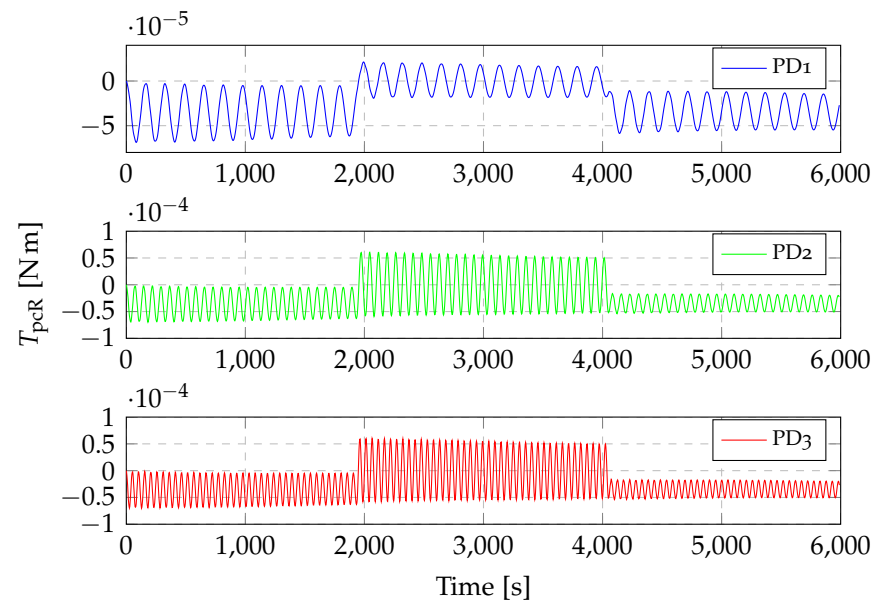


Figure 4.22: Control torques exerted by the control system on the connecting joint between the right panel and the central body (see table 4.5).

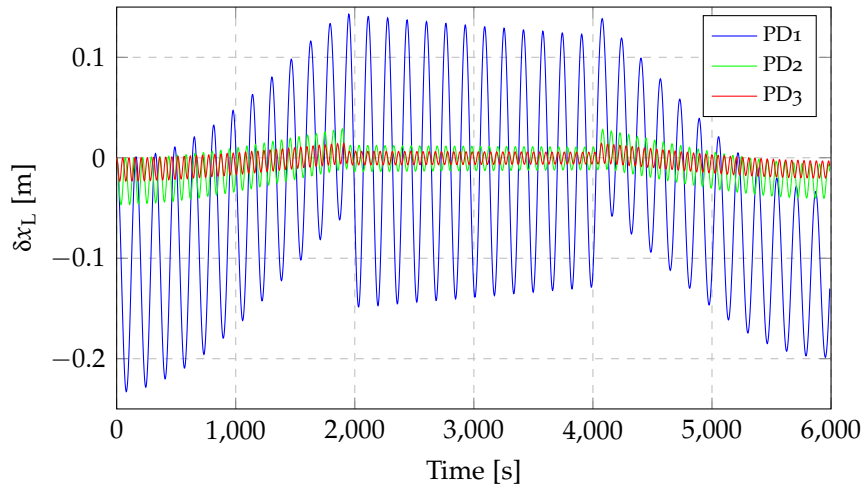


Figure 4.23: Displacements of the left tip at 750 km altitude with nadir pointing attitude with controlled systems (see table 4.6).

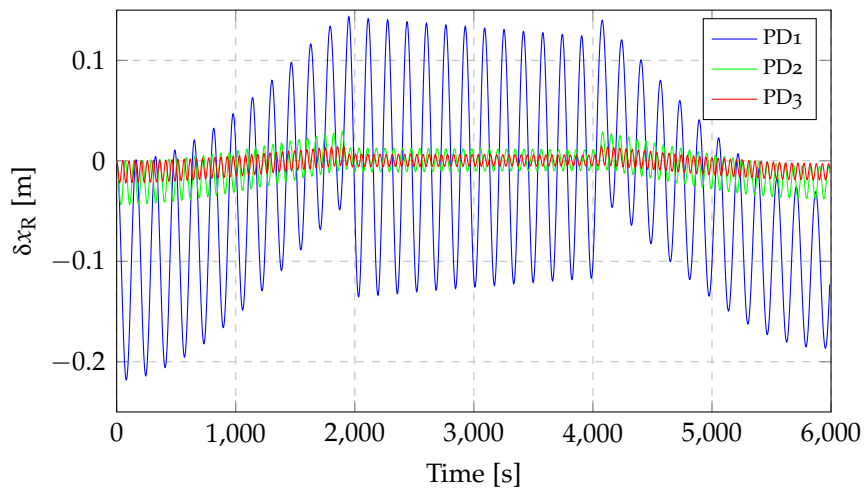


Figure 4.24: Displacements of the right tip at 750 km altitude with nadir pointing attitude with controlled systems (see table 4.6).

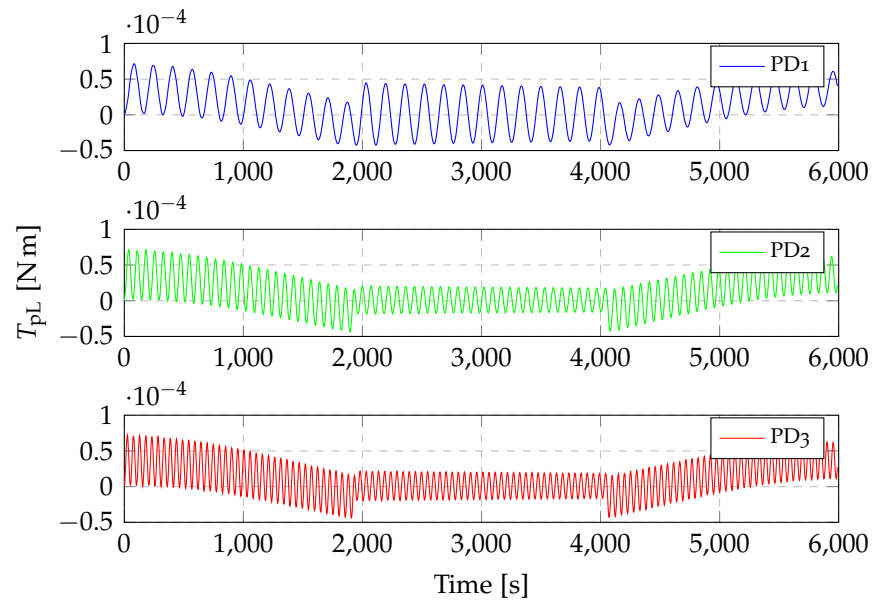


Figure 4.25: Torques transferred from the left panel to the central body at 750 km altitude with nadir pointing attitude (see table 4.6).

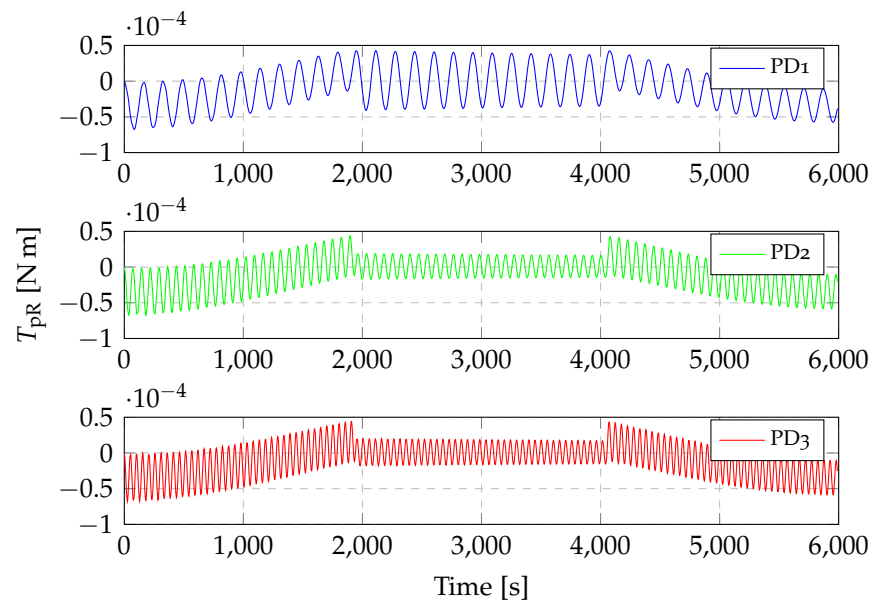


Figure 4.26: Torques transferred from the right panel to the central body at 750 km altitude with nadir pointing attitude (see table 4.6).

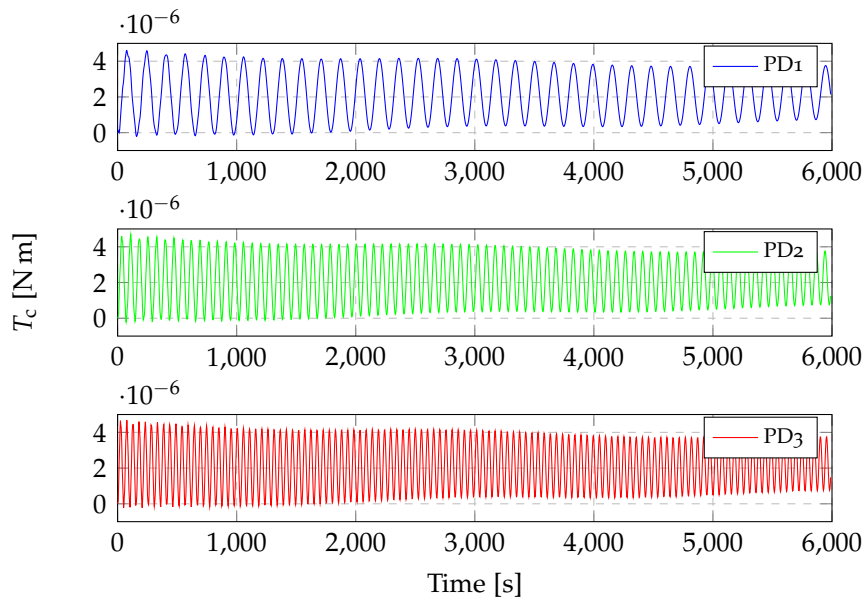


Figure 4.27: Control torques on the satellite at 750 km altitude with nadir pointing attitude (see table 4.6).

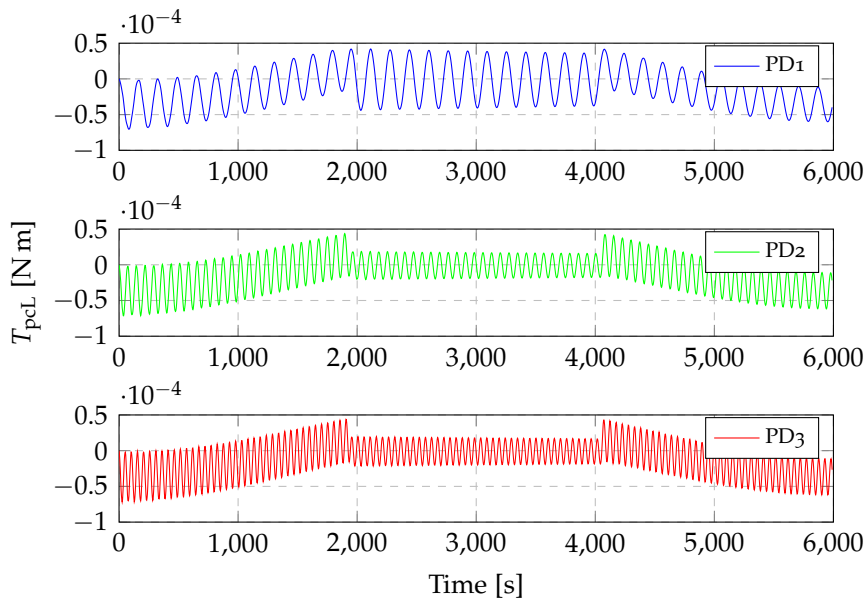
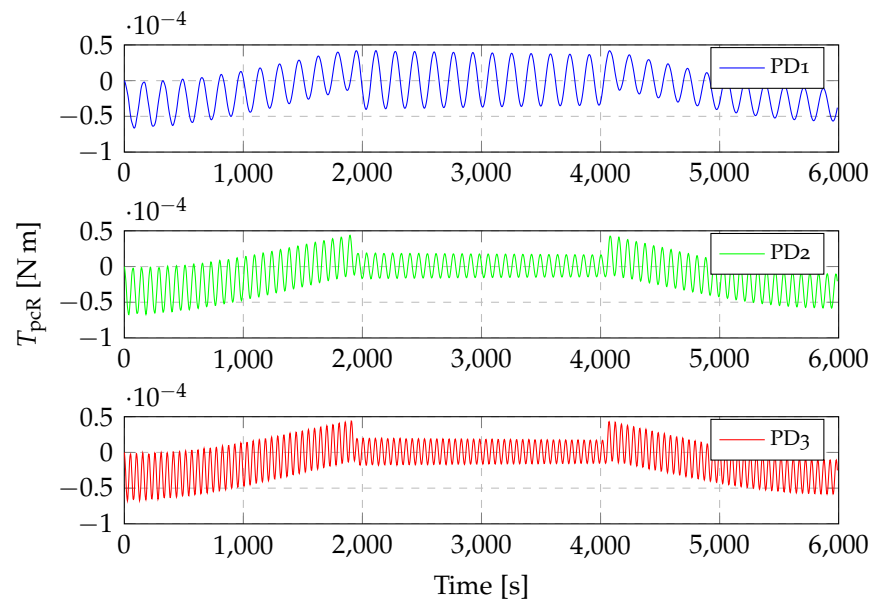


Figure 4.28: Control torques exerted by the control system on the connecting joint between the left panel and the central body (see table 4.6).



**Figure 4.29:** Control torques exerted by the control system on the connecting joint between the right panel and the central body (see table 4.6).

# 5

## COMPARISON BETWEEN THE SIMULATED SYSTEMS

In order to establish which is the best choice between a stiffened and an actively controlled system, some significant parameters are compared in this chapter.

### 5.1 TORQUES

The first and principal comparison between the two systems is made analyzing the torques necessary for the control system of the central body to keep the nominal pointing. This system commonly consists on a set of reaction wheels, which are typically heavy with respect to the total mass of the satellite if the torques to counteract are relatively high.

In the figures from 5.1 to 5.4, these comparisons are reported, taking into account only the stiffened configurations which are of practical interest:

- in low LEO, only the stiffened configuration with 500  $\mu\text{m}$  thick panels;
- in high LEO, both the configurations with 200  $\mu\text{m}$  and 500  $\mu\text{m}$  panel cross sections.

In all of the figures, the systems with stiffened panels are compared with the three simulated cases of actively controlled systems. The reported displacements are referred to the left panel tip.

In figures 5.1 and 5.2, relative to the simulations in low LEO, it is evident that the torques needed by the central body to keep the nominal pointing are related to the displacements of the panel tip. In the following two figures 5.3 and 5.4, showing the results in high LEO, the torques required to keep the nominal pointing of the central body clearly increase with the stiffening of the panels. This is principally due to the fact that the gravity gradient force increases with the mass of the panel,

while the force due to the solar radiation does not vary significantly between the considered configurations, since it is highly dependent on the deformations of the panels.

The most excited system is the nadir-pointing satellite in low LEO (figure 5.2), where the control torques on the central body reach the order of  $10^{-3}$  N m. For this system, an example of reaction wheel which is able to provide 10 mNm of control torque weights typically around 1 kg (from *Microwheel 10SP-M* datasheet, Surrey Satellite Technology Ltd.). Reducing the requested authority of the control system of the central body and using a set of smaller reaction wheels results in considerable mass savings especially in a small satellite.

Anyway, in all the figures the performances of the actively controlled systems improve, reducing the needed torques on the central body with respect to the stiffened configurations, which in high LEO reach one order of magnitude less with respect to the stiffened configuration.

Concluding, comparing the behavior of the central body in terms of torques requested to keep the nominal pointing, the actively controlled systems bring benefits while increasing the authority of the control systems of the panels.

## 5.2 MASS

In a small satellite, mass savings is of fundamental importance. Therefore, the second analysis is made comparing the mass of the different panels configurations.

The mass of the system increases significantly with respect to the controlled configuration with 25  $\mu$ m thick panels as shown in table 2.4. The difference between the masses of the controlled and the stiffened configurations are reported in table 5.1 as well as the percentage difference referred to the mass increase in each case. A configuration with 500  $\mu$ m thick solar arrays is 19 times heavier than two 25  $\mu$ m panels.

*Is the control system of the panels sufficiently light to not exceed the difference in terms of mass between the stiffened and the active controlled configurations?* This question can be precisely answered only knowing the exact architecture of the control system.

In figures 5.5 and 5.6 the mass of the solar arrays is correlated to the displacements of the panel tips respectively in low and high LEO. The first two columns of figure 5.5 and the first and third columns of figure 5.6 show a similar displacement of the

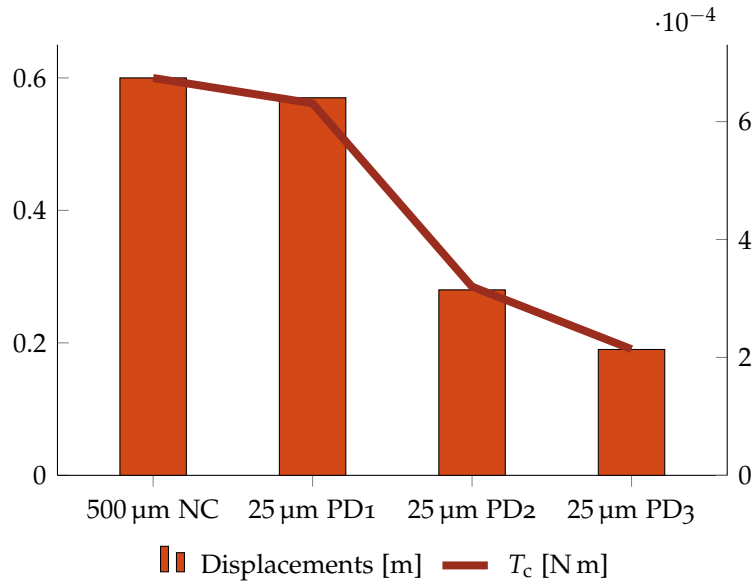


**Figure 5.1:** Comparison between the displacements and the torques needed to control the satellite in the stiffened case with 500  $\mu\text{m}$  thick panels and three entirely controlled systems in low LEO with inertial attitude.

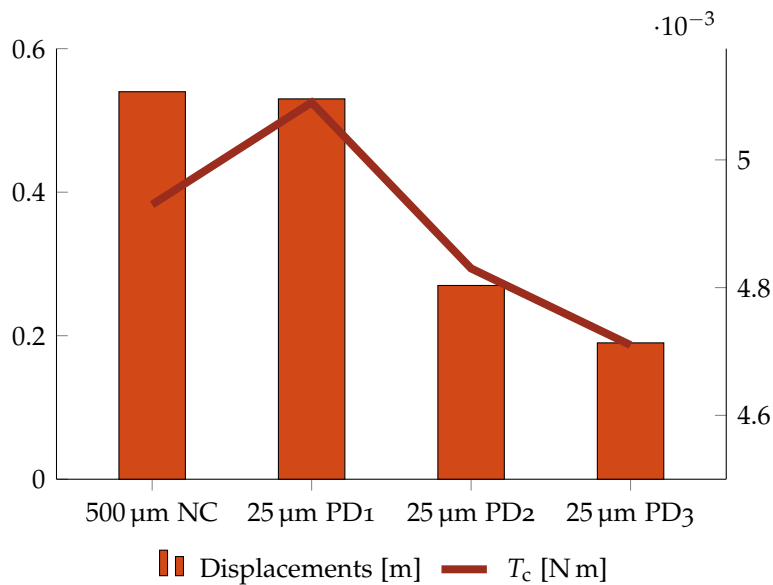


**Figure 5.2:** Comparison between the displacements and the torques needed to control the satellite in the stiffened case with 500  $\mu\text{m}$  thick panels and three entirely controlled systems in low LEO with nadir pointing attitude.

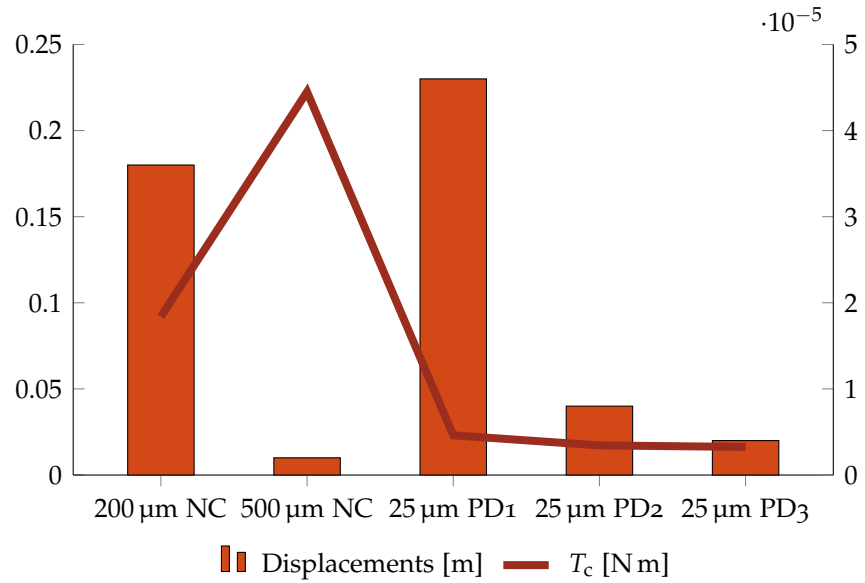


**Figure 5.3:** Comparison between the displacements and the torques needed to control the satellite in the stiffened cases with 200  $\mu\text{m}$  and 500  $\mu\text{m}$  thick panels and three entirely controlled systems in high LEO with inertial attitude.

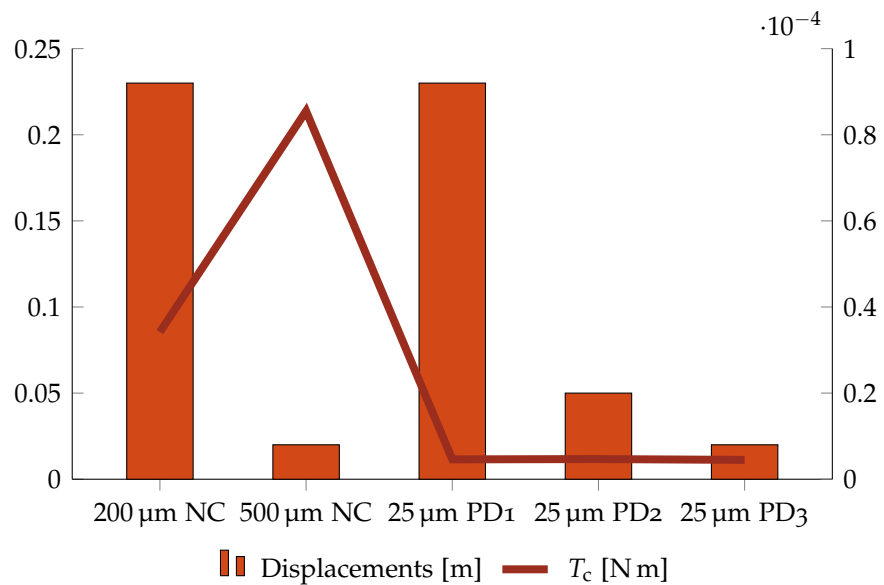


**Figure 5.4:** Comparison between the displacements and the torques needed to control the satellite in the stiffened cases with 200  $\mu\text{m}$  and 500  $\mu\text{m}$  thick panels and three entirely controlled systems in high LEO with nadir pointing attitude.

$s$ [ $\mu\text{m}$ ]	CF1	CF2	%
100	0.459	0.483	300
200	1.072	1.127	700
500	2.908	3.060	1900

**Table 5.1:** Difference between the masses (in kg) of the different stiffened configurations (in CF1 the panel length is 5.39 m, in CF2 it corresponds to 5.67 m) and the 25  $\mu\text{m}$  thick panels. In the last column, the percentage difference is reported.

panel tips, but an important mass reduction in the controlled system.

On the other side, in figures 5.7 and 5.8 a comparison is made between the control torques required to the control system of the central body and the mass of the respective configurations. While in low LEO torques are related to the displacements of the panel tips, figure 5.8 shows that in high LEO the control torques needed to keep the nominal pointing of the central body are closely related to the mass of the panels. This is due to the fact that in high LEO the gravity gradient force, which is dependent on the mass of the system, assume an important role with respect to the other disturbances.

The advantage in terms of mass is significant on the actively controlled systems. However, if an active control system is implemented, the mass of the controller has to be taken into account. This means that if the control system of the panels is lighter with respect to the mass increasing of a stiffened configuration, its application on a small satellite brings sure benefits, while on a large satellite the gain in terms of mass savings becomes irrelevant.

## 5.3 REQUIRED POWER

While the satellite itself needs a control system to be kept at nominal pointing both when the panel is active controlled and when it is stiffened, an active system for controlling the panels requires an additional amount of power to be effective.

A qualitative analysis can be made again analyzing figures from 5.1 to 5.4 and 5.7–5.8. They show that the torques on the central body in systems with controlled panels are lower than in stiffened systems, both in low and in high orbits. This advan-

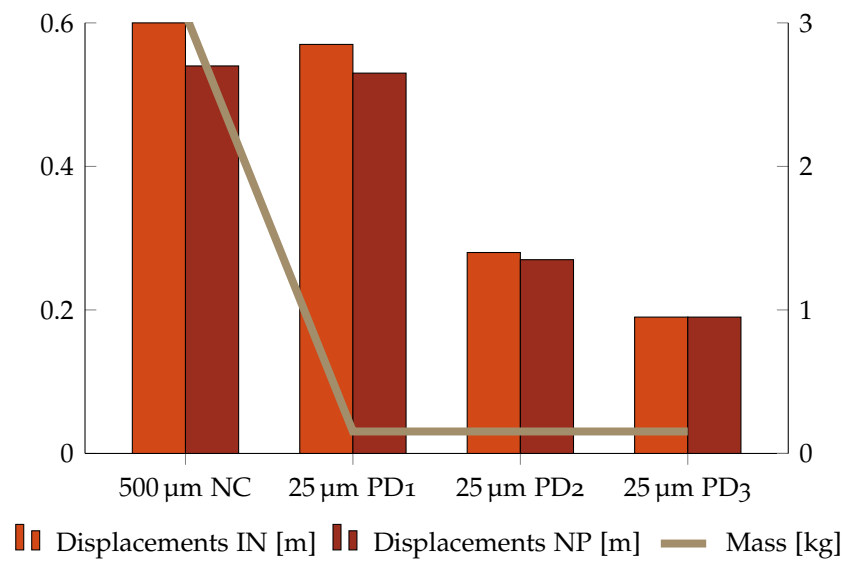


**Figure 5.5:** Comparison between the displacements and the masses of the systems in the stiffened case with 500  $\mu\text{m}$  thick panels and three entirely controlled systems in low LEO.

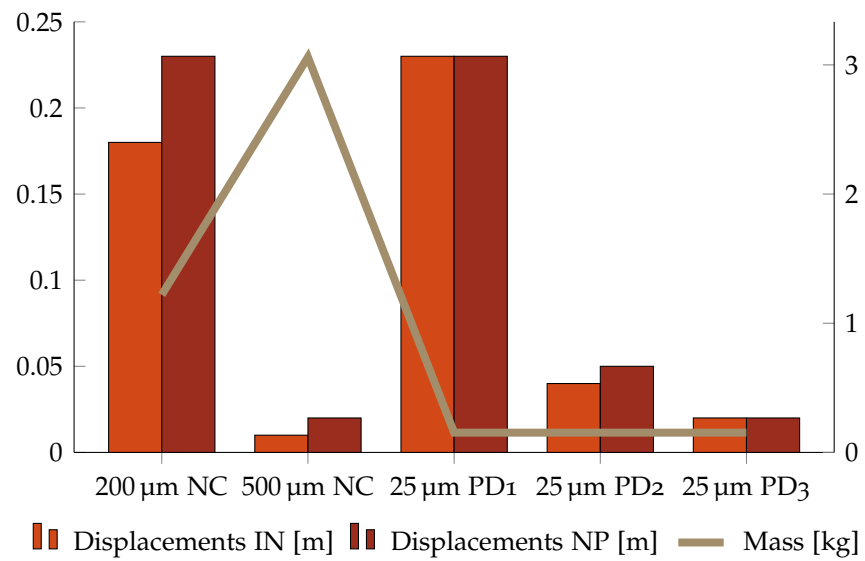


**Figure 5.6:** Comparison between the displacements and the masses of the systems in the stiffened case with 200  $\mu\text{m}$  and 500  $\mu\text{m}$  thick panels and three entirely controlled systems in high LEO.

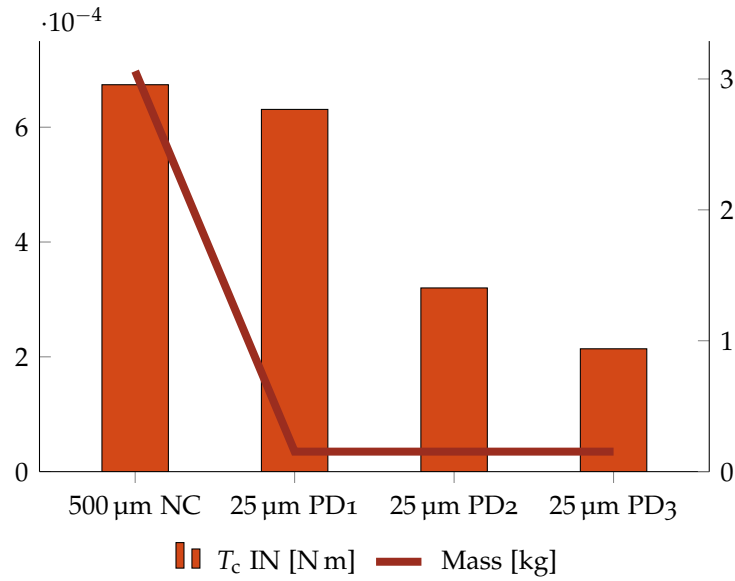


**Figure 5.7:** Comparison between the control torques and the masses of the systems in the stiffened case with 500  $\mu$ m thick panels and three entirely controlled systems in low LEO with inertial attitude.

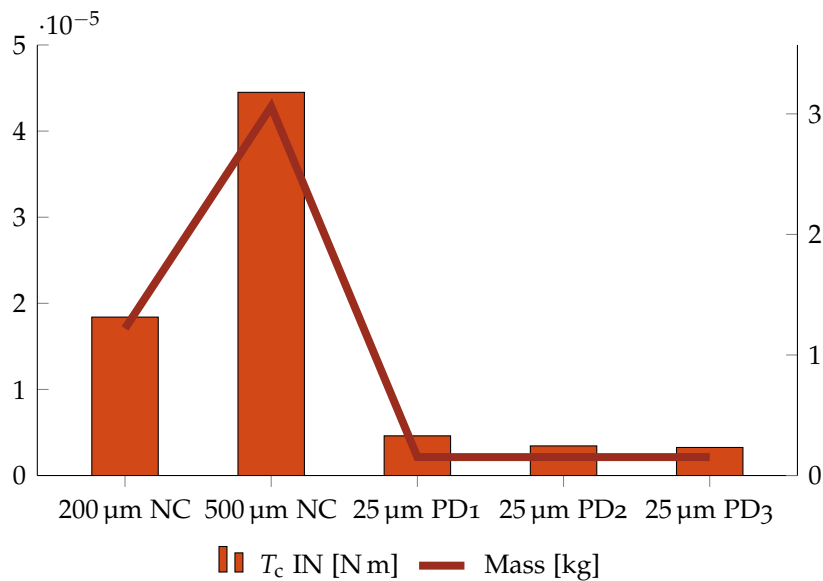


**Figure 5.8:** Comparison between the control torques and the masses of the systems in the stiffened case with 200  $\mu$ m and 500  $\mu$ m thick panels and three entirely controlled systems in high LEO with inertial attitude.

tage translates into savings in the power expense for the control system of the central body, since the modulus of the torques that have to be counteracted is lower. This allows an undersized control system of the central body, which is typically composed by a set of reaction wheels. A reaction wheel with 10 mNm of nominal torque could possibly consume 11.5 W to work at nominal speed (from *Microwheel 10SP-M* datasheet, Surrey Satellite Technology Ltd.).

*Does the power requested from the entire system with actively controlled panels exceed the power necessary on a stiffened system?*

The question could be more precisely answered if the model of the control system was known. However, the lower the power requirements, the higher the advantages in making use of an active control system on the panels.

# 6

## PROPOSAL OF AN INNOVATIVE CONTROL SYSTEM

In a thin and light structure such as thin-film solar panels, the vibration control system must be the least invasive possible in terms of mass and volume, in order to minimize its influence on the overall structure and maintain the savings on the mass budget.

In order to answer the questions of the previous chapter, a control system with low mass and power requirements, and able to exert sufficiently high forces is sought.

In recent years, smart structures and active materials have been studied and have been used in a variety of fields, from aerospace to robotics. Smart structures typically consist of a host structure incorporated with sensors and actuators coordinated by a controller. They have the ability to perform self-diagnosis and adapt to the environmental changes. Sensors and actuators are typically patches of smart materials, such as for instance shape memory alloys (SMAs), piezoelectric ceramics/polymers, magnetostrictive materials and electroactive polymers (EAPs). In contrast to conventional transducers, these actuators are not mechanically complex since they do not consist of many interacting parts; this characteristic makes them more suitable for being used on thin and very flexible structures.

Two possible candidate materials for solar arrays control purpose are briefly presented in the following paragraphs.

### 6.1 PIEZOELECTRIC POLYMERS

Piezoelectric materials are the most widely known and used smart materials, because they have reached their maturity over the last decades.

Many studies have been done so far on the control of flexible beams and plates using piezoelectric materials. However,

the dimensions and cross sections of the controlled structure do not match the sizes of the system studied in this work. In particular, typical structure cross sections exceed 1 mm. In addition to this, commonly piezo-ceramic materials are used (see for example [31]).

Optimal placement of piezoelectric patches on flexible structures is presented in [32]. Bending deformations are better counteracted by patches of piezoelectric material placed opposite with respect of the panel tip whose larger dimension is along the length of the structure. On the other hand, torsional deformations are better controlled if the patches are located near the tip of the structure and oriented at  $45^\circ$  with respect to the axial direction.

Piezoelectric polymers share with piezoceramics the same working principle. If they are subjected to a mechanical stress, they develop a proportional electrical charge, while if an electrical field is applied, they show an internal generation of mechanical strain.

Piezo-films are commonly made of PVDF (polyvinylidene fluoride), which is a light ( $\rho = 1780 \text{ kg/m}^3$ ), highly stable and mechanically strong ferroelectric material, with a high operative frequency range (0.001 to  $10^8 \text{ Hz}$ ). This patches can be directly attached to the structure without disturbing its mechanical motion. Typical thicknesses are in the range of 9–110  $\mu\text{m}$ , but copolymers reach cross sections of less than 1  $\mu\text{m}$ . These thicknesses are compatible with thin-film panels dimensions. In addition to this, large areas patches are available (from *Piezo Film Sensors Technical Manual*, Measurement Specialties, Inc.).

Another advantage of this technology is related to its very low power consumption. A piezo-film works as a capacitor, hence current flows only if there is motion. If the panel is controlled, its deformations are limited. This means that a low



Figure 6.1: An example of piezo-film, from [www.meas-spec.com](http://www.meas-spec.com).

amount of current flows in the circuits and, as a consequence, a very low amount of power is needed.

The same working principle and materials are also typical of piezo-cables, which could be used as sensors/actuators as well as piezoelectric films.

## 6.2 DIELECTRIC ELASTOMERS

Dielectric elastomers are a relatively soft and dry electroactive materials, with low density ( $\rho = 1000\text{--}2500 \text{ kg/m}^3$ ). In addition to this, they are resilient and fracture tolerant.

They exploit the electrostatic Maxwell stress experienced by all dielectrics. The actuation of this device is performed by the application of electrostatic forces between two electrodes attached to the polymer film, which behaves essentially like a capacitor. Applying the voltage, the opposite charges the opposite electrodes tend to attract each other. Therefore, the polymer is squeezed in the direction parallel to the electric field, and since rubber is highly deformable but incompressible (with a Poisson's ratio of about 0.5), this leads to an expansion of the area of the polymer film in the directions normal to the electric field.

Moreover, the like charges tend to repel each other leading to an expansion of the electrode, which do not oppose to the deformation thanks to its inherent nature. The relation between the force and the electric field  $E$  is expressed by the equation:

$$f = \epsilon\epsilon_0 A E^2 \quad (6.1)$$

where  $A$  is the area and  $\epsilon$  is the relative dielectric constant. The stress developed ( $f/A$ ) is called *Maxwell stress* [33]. There is a built-in amplification process since as the film cross sec-

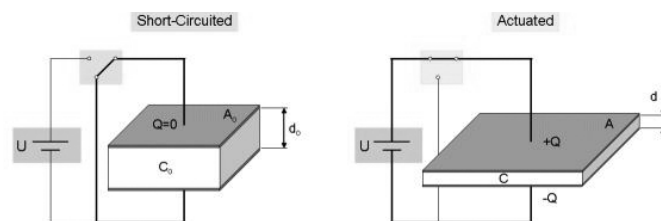


Figure 6.2: Working principle of dielectric elastomers.

tion reduces, the electric field modulus increases. According to equation (6.1), the actuation is non-linear, with a deformation approximately proportional to the square of the applied voltage. Dielectric elastomers are noiseless actuators, capable of very high strains, requiring a large actuation voltage to produce high electric fields (10 to 150 V/ $\mu\text{m}$ ), but very low electrical power consumption (mW) [34, 35]. This is due to the same reason reported for the piezoelectric polymers, i.e. if the strains are limited, low current flows, thus low amount of power is needed.

Typical dielectric elastomers based on silicon-oxygen polymers appear to be usable over an extended temperature range, between 173 K and 553 K. Strains of 380% and 63% have been observed in acrylic and silicate based systems respectively, exerting pressures of 3.0 to 7.2 MPa [33]. Another advantage of this system is represented by its very fast reaction speed.

A challenge limit of this system is due to the fact that better performances are achievable with pre-strained polymers: when film thickness is reduced, a lower voltage is required for the same electrostatic pressure. In the case of application on thin films, a support structure should be added to the system to avoid the collapse of the material. However, if a proper geometry is designed, dielectric elastomers could be an effective means to damp oscillations on thin-film power systems.

# 7 | CONCLUSION

This thesis presents the results of dynamic analysis of thin-film solar panels in LEO environment.

Many efforts have been done to reduce the overall mission costs. Every system is being miniaturized, but the power subsystem have to be large enough to equip sufficient power to the satellite. Providing the satellite with thin-film solar panels the mass of the system reduce significantly, but the inherent high flexibility of the panels brings to unavoidable large deformations. Stiffening the panel or providing the panels with a control system can be the solution, without adding mass and complexity associated to the deployment of typical booms. Which is the best alternative?

According to the results of the performed simulations, a control system on the panels brings benefits to the behavior of the central body. The torques needed to keep the satellite at the nominal pointing reduce, therefore its attitude control system (typically reaction wheels) can be undersized with respect to the stiffened system. In addition to this, the mass of a controlled system allows a lighter satellite, reducing the total mass budget. Piezoelectric patches or wires as well as other electroactive materials bonded to the panel could be able to provide an effective control on the system, damping unwanted vibrations and reducing the displacements of the panels tips. Their lightness and low power requirements offer the possibility of maintaining the advantages of thin modules, such as low mass, low stowage volume, high power density etc. Nevertheless, the mass reduction of a controlled system is more significant in a small satellite. On the contrary, on a large satellite the mass penalty due to the increasing of the thickness of a stiffened panel becomes irrelevant.

Future work will address the behavior of panels subjected to typical maneuvers. In addition to this, other simulations can be performed on modules with different geometries.

Additional studies on the possibility of controlling the panels with smart materials will be done. After a more in-depth feasibility study, the most promising material should be chosen and an experimental setup of the proposed strategy could be realized. Furthermore, a deployment system could be simulated and designed.



## BIBLIOGRAPHY

- [1] Peter A. Iles. "Evolution of space solar cells". In: *Solar Energy Materials and Solar Cells* (2001) (cit. on pp. 1, 2).
- [2] Karsten Otte et al. "Flexible Cu(In,Ga)Se<sub>2</sub> thin-film solar cells for space application". In: *Thin Solid Films*. Ed. by Elsevier B.V. 511–512 vols. 2006, pp. 613–622 (cit. on pp. 2, 3).
- [3] J.W. Tringe. "Trends in thin film photovoltaic technology development for space application". In: *Aerospace Conference Proceedings*. Ed. by IEEE. Vol. 4. Big Sky, MT, 2000, pp. 61–68 (cit. on pp. 2, 4, 8).
- [4] Sheila Bailey and Ryne Raffaele. *Handbook of Photovoltaic Science and Engineering*. 2003 (cit. on pp. 2–4, 8).
- [5] James R Woodyard and JG Severns. "Analysis of LIPS III satellite a-Si: H alloy solar cell data". In: *Photovoltaic Specialists Conference, 1996., Conference Record of the Twenty Fifth IEEE*. IEEE. 1996, pp. 263–266 (cit. on p. 3).
- [6] Henry Curtis and D Marvin. "Final Results from the PASP Plus Flight Experiment". In: *Photovoltaic Specialists Conference, 1996., Conference Record of the Twenty Fifth IEEE*. IEEE. 1996, pp. 195–198 (cit. on p. 3).
- [7] T. Yee. "Roadrunner, a High-Performance Responsive Space Mission". In: *AIAA/USU Conference on Small Satellites*. Logan, UT, Aug. 2004 (cit. on p. 3).
- [8] Paul E Hausgen et al. "AFRL thin-film photovoltaics DSX and roadrunner flight experiments". In: *Photovoltaic Specialists Conference, 2005. Conference Record of the Thirty-first IEEE*. IEEE. 2005, pp. 614–617 (cit. on p. 3).
- [9] K. L. Chopra, P. D. Paulson, and V. Dutta. "Thin-Film Solar Cells: An Overview". In: *Prog. Photovolt: Res. Appl.* (2004), pp. 69–92 (cit. on pp. 3, 4).
- [10] Mario Pagliaro, Giovanni Palmisano, and Rosaria Ciriminna. *Flexible Solar Cells*. John Wiley & Sons, 2008 (cit. on p. 3).
- [11] Lewis M Fraas and Larry D Partain. *Solar cells and their applications*. Vol. 236. Wiley. com, 2010 (cit. on p. 4).

- [12] Gang Li, Rui Zhu, and Yang Yang. "Polymer solar cells". In: *Nature Photonics* (Mar. 2012) (cit. on p. 4).
- [13] Kai Zajac et al. "New findings of the German joint project flexible CIGSe thin film solar cells for space flight". In: *Photovoltaic Specialists Conference (PVSC), 2009 34th IEEE*. IEEE. 2009, pp. 000055–000059 (cit. on p. 5).
- [14] J. Tringe, J. Merrill, and K. Reinhardt. "Developments in thin-film photovoltaics for space". In: *Photovoltaic Specialists Conference*. Ed. by IEEE. Anchorage, AK, 2000, pp. 1242–1245 (cit. on p. 5).
- [15] EL Ralph. "High efficiency solar cell arrays system trade-offs". In: *Photovoltaic Energy Conversion, 1994., Conference Record of the Twenty Fourth. IEEE Photovoltaic Specialists Conference-1994, 1994 IEEE First World Conference on*. Vol. 2. IEEE. 1994, pp. 1998–2001 (cit. on p. 5).
- [16] David J Hoffman et al. "Thin-film photovoltaic solar array parametric assessment [space power]". In: *Energy Conversion Engineering Conference and Exhibit, 2000.(IECEC) 35th Intersociety*. Vol. 1. IEEE. 2000, pp. 670–680 (cit. on p. 5).
- [17] Patrick Reinhard et al. "High efficiency flexible Cu (In, Ga) Se<sub>2</sub> solar cells". In: *Active-Matrix Flatpanel Displays and Devices (AM-FPD), 2013 Twentieth International Workshop on*. IEEE. 2013, pp. 79–82 (cit. on p. 6).
- [18] A. Jasenek and U. Rau. "Defect generation in Cu(In,Ga)Se<sub>2</sub> heterojunction solar cells by high energy electron and proton irradiation". In: *J. Appl. Phys.* 90.2 (2001), pp. 650–658 (cit. on p. 6).
- [19] DL Bätzner et al. "Radiation hardness of CdTe/CdS solar cells". In: *17th PVSEC, Munich, OA9 3* (2001) (cit. on p. 6).
- [20] A Romeo et al. "Potential of CdTe thin film solar cells for space applications". In: *17th European Photovoltaic Solar Energy Conference*. 2001, pp. 2183–2186 (cit. on p. 6).
- [21] S.H. Liu et al. "Thin-Film Photovoltaic Radiation Testing for Space Applications". In: *Photovoltaic Energy Conversion*. Ed. by IEEE. Vol. 2. 2006 (cit. on p. 6).
- [22] Neelkanth G Dhere et al. "CIGS<sub>2</sub> thin-film solar cells on flexible foils for space power". In: *Progress in Photovoltaics: Research and Applications* 10.6 (2002), pp. 407–416 (cit. on p. 8).

- [23] Simon H. Liu et al. "Evaluation of Thin-film Solar Cell Temperature Coefficients for Space Applications". In: *Prog. Photovolt: Res. Appl.* (2005) (cit. on p. 8).
- [24] A Virtuani, D Pavanello, and G Friesen. "Overview of temperature coefficients of different thin film photovoltaic technologies". In: *25th European Photovoltaic Solar Energy Conference and Exhibition/5th World Conference on Photovoltaic Energy Conversion*. 2010, pp. 6–10 (cit. on pp. 8, 9).
- [25] DongXu Li, Wang Liu, and JianPing Jiang. "The influence of orbital motion of flexible space vehicle on the dynamic traits of solar panel". In: *International Conference on Communications, Computing and Control Applications (CCCA), 2011*. IEEE. 2011, pp. 1–5 (cit. on p. 9).
- [26] Cary Clark, Jason Wood, and Bill Zuckerman. "Self Deploying, Thin-Film PV Solar Array Structure". In: *Proceedings of the AIAA/USU Conference on Small Satellites*. 2002 (cit. on p. 10).
- [27] Edward J Simburger et al. "Advancements in the development of thin film amorphous silicon space solar cell for the PowerSphere concept". In: *Photovoltaic Specialists Conference, 2000. Conference Record of the Twenty-Eighth IEEE*. IEEE. 2000, pp. 1053–1056 (cit. on p. 10).
- [28] Deliana Ernst. "Beam It Down, Scotty: The Regulatory Framework for Space-Based Solar Power". In: *Review of European, Comparative & International Environmental Law* 22.3 (2013), pp. 354–365 (cit. on p. 10).
- [29] David A Vallado. *Fundamentals of astrodynamics and applications*. Vol. 12. Springer, 2001 (cit. on p. 23).
- [30] Computer Sciences Corporation. Attitude Systems Operation and J.R. Wertz. *Spacecraft Attitude Determination and Control*. Astrophysics and Space Science Library : a series of books on the recent developments of space science and of general geophysics and astrophysics. Reidel, 1978. ISBN: 9789027709592 (cit. on p. 27).
- [31] Zhi-cheng Qiu et al. "Active vibration control of a flexible beam using a non-collocated acceleration sensor and piezoelectric patch actuator". In: *Journal of sound and vibration* 326.3 (2009), pp. 438–455 (cit. on p. 74).

- [32] Zhi-cheng Qiu et al. "Optimal placement and active vibration control for piezoelectric smart flexible cantilever plate". In: *Journal of Sound and Vibration* 301.3 (2007), pp. 521–543 (cit. on p. 74).
- [33] R.H.C. Bonser et al. *EAP-Based artificial muscles as an alternative to space mechanisms*. Tech. rep. The University of Reading, Whiteknights, Reading RG6 2AY, 2004 (cit. on pp. 75, 76).
- [34] Yoseph Bar-Cohen et al. *Electroactive polymer (EAP) actuators as artificial muscles: reality, potential, and challenges*. Vol. 5. SPIE press Bellingham, WA, 2004 (cit. on p. 76).
- [35] Ailish OHalloran, Fergal OMalley, and Peter McHugh. "A review on dielectric elastomer actuators, technology, applications, and challenges". In: *Journal of Applied Physics* 104.7 (2008), p. 071101 (cit. on p. 76).

## RINGRAZIAMENTI

Alla fine di questo lungo lavoro, desidero ringraziare il mio relatore, prof. Alessandro Francesconi, per la disponibilità con cui mi ha seguita in questo periodo di tesi.

Un ringraziamento speciale va al correlatore Francesco Branz, che è riuscito a sopportarmi, a incoraggiarmi e ad insegnarmi molte cose in questi mesi. Senza di lui questa tesi non sarebbe quello che è. Grazie, davvero.

Devo molto anche al mio amico Davide, che mi è stato molto d'aiuto nell'impaginazione del documento. Grazie di cuore!

Infine, voglio ringraziare sinceramente i miei amici vecchi e nuovi, soprattutto Annagiulia, e la mia famiglia, che mi sono stati vicini e mi hanno sempre incoraggiata spronandomi a fare del mio meglio.